KASTAMONU UNIVERSITY JOURNAL OF ENGINEERING AND SCIENCES

e-ISSN 2667-8209

VOL: 09 ISSUE:01

KASTAMONU UNIVERSITY JOURNAL OF ENGINEERING AND SCIENCES

e-ISSN 2667-8209

Kastamonu University Journal of Engineering and Science

Kastamonu University Journal of Engineering and Science publish as blind peer review and two times in a year.

Kastamonu University
Journal of Engineering and Science

Vol: 9 Issue: 1 June 2023 E-ISSN:2667-8209

Kastamonu University
Journal of Engineering and Science

Vol: 9 Issue: 1 June 2023 E-ISSN:2667-8209

Kastamonu University Faculty of Engineering and Architecture 37150 Kastamonu / TÜRKİYE
Tel: +(90)366 2802901 Fax: +(90)366 2802900

Web: https://dergipark.org.tr/tr/pub/kastamonujes
e-mail: kujes@kastamonu.edu.tr

This journal is published two times in a year.
June and December
Kastamonu University Journal of Engineering and Science
Indexed and Abstracted in: Dergipark

Kastamonu University
Journal of Engineering and Science

Vol: 9 Issue: 1 June 2023 E-ISSN:2667-8209

CONTENTS

doi:10.55385/kastamonujes.1285522 KUJES 9(1):1-9, 2023

Kastamonu University
Journal of Engineering and Sciences
e-ISSN 2667-8209
http://dergipark.gov.tr/kastamonujes

Effect of Drought and UV-B Stress on Stoma Characteristics in Two Maple Species

Hatice Çobanoğlu[a, *], Şemsettin Kulaç[b], Hakan Şevik[c]

[a] Düzce University, GraduateSchool of Natural and Applied Sciences, Faculty of Forestry, Department of Forest Engineering, Düzce, Türkiye
[b] Duzce University, Department of Forest Engineering, Düzce, Türkiye
[c] Kastamonu University, Environmental Engineering Department, Faculty of Engineering and Architecture, Türkiye
***Corresponding Author:** haticecobannoglu@gmail.com

Received: **April 24, 2023** ◆ Accepted: **June 5, 2023** ◆ Published Online: **June 21, 2023**

Abstract: In recent years, changing climatic conditions have brought along many problems. As a result of the increasing destruction of the ozone layer caused by anthropogenic sources, the effect of harmful sun rays reaching our world is increasing. It is estimated that the temperatures on the earth's surface and ultraviolet-B (UV-B) radiation will increase in the coming years due to global climate change. This study used ash-leaved maple (*Acer negundo* L.) and sycamore maple (*Acer pseudoplatanus* L.) seedlings to examine the effects of drought and UV-B radiation levels that may occur in the coming years on forest trees. The study investigated the effect on stomatal characters by applying two different doses of UV-B and drought stress. As a result of the study, it was determined that UV-B stress had a more significant effect on stomatal characters than drought stress. It has been observed that severe drought generally reduces the number of stomata. It was determined that the sycamore maple was more affected by severe drought and UV-B radiation. While UV-B radiation decreased only the stomatal pore length and width in sycamore maple, it increased the stomatal pore length and width in ash-leaved maple. The response of stomatal characters to drought and UV-B stress remains unclear. Therefore, more detailed studies are required.

Keywords: Stoma, drought stress, UV-B radiation, *Acer negundo* L., *Acer pseudoplatanus* L.

Öz: Son yıllarda değişen iklim koşulları beraberinde birçok sorunu da ortaya çıkarmıştır. Antropojenik kaynakların neden olduğu ozon tabakasındaki tahribatın gittikçe artması sonucunda dünyamıza ulaşan zararlı güneş ışınlarının etkisi de giderek artmaktadır. Gelecek yıllarda dünya yüzeyindeki sıcaklıklarının 1-2 °C artarak daha sıcak olması beklenmektedir. Bundan dolayı kuraklık ve UV-B radyasyon zararının gözle görünür şekilde olacağı beklenmektedir. Bu çalışmada oluşabilecek kuraklık ve UV-B radyasyon seviyelerinin orman ağaçları üzerindeki etkisini incelemek için Dişbudak yapraklı akçaağaç ve Dağ akçaağacı türleri kullanılmıştır. Çalışmada iki farklı doz UV-B ve kuraklık stresi uygulanarak stomatal karakterler üzerindeki etkisi araştırılmıştır. Çalışma sonucunda UV-B stresinin kuraklık stresine göre stoma karakterleri üzerinde daha fazla etkisi olduğu belirlenmiştir. Şiddetli kuraklığın genel olarak stoma sayısını azalttığı gözlenmiştir. Dağ akçaağacı türünün hem şiddetli kuraklık hem de UV-B radyasyonundan daha fazla etkilendiği belirlenmiştir. Sadece UV-B radyasyonun Dağ akçaağacında stoma por boyunu ve enini azaltırken, Dişbudak yapraklı akçaağaç türünde stoma por boyunu ve enini arttırdığı görülmüştür. Stomatal karakterlerin kuraklık ve UV-B stresine karşı tepkileri belirsizliğini hala korumaktadır. Bundan dolayı daha detaylı çalışmaların yapılması gerekmektedir.

Anahtar Kelimeler: Stoma, kuraklık stresi, UV-B radyasyonu, *Acer negundo* L., *Acer pseudoplatanus* L.

1. Introduction

Ultraviolet-B (UV-B) radiation intensities between 280 and 320 nm in the biosphere have increased due to the depletion of the stratospheric ozone layer catalyzed by chlorofluorocarbons and other anthropogenic contaminants [1-2]. UV-B levels reaching the Earth's surface are highly dynamic and are determined by time of day, altitude, latitude, season, shade, and various other factors. How plants adapt to changing UV-B levels and coordinate growth and UV-B stress responses has yet to be fully understood [3]. UV-B radiation has numerous direct and indirect effects on plants, including pollination, transpiration, damage to proteins, DNA, and membranes, changes in photosynthesis and transpiration, and changes in morphology, growth, and development [2], [4-5]. In addition, UV-B radiation can reduce photosynthetically active radiation (PAR) penetration, impair stomatal function, photosynthetic and auxiliary pigments and adjust canopy morphology, thereby indirectly delaying photosynthetic carbon assimilation [6].

UV-B radiation is estimated to increase significantly in the coming years due to global climate change [7-8]. Global climate change, accepted as the most critical global and irreversible problem today [9-11], is a process that will affect all living things and ecosystems on Earth [9], [12-13]. It is stated that the most important effects of global climate change will manifest themselves as an increase in drought [14-15].

Drought stress is one of the most critical stress factors that plants are exposed to and affects plant metabolism in many ways [16-18]. Some studies show that drought stress causes significant changes in plants at the micromorphological level [19-20]. However, it is stated that drought stress has different effects on different plant species [21], and these effects occur primarily at the invisible micromorphological level [22]. Similarly, UV-B stress causes many morphological and physiological changes in plants [23]. However, the number of studies on the possible effects of drought and UV-B stress, considered the most prominent effects of global climate change, on plants is limited. This study investigated the responses of plant stomata characters under drought and UV-B stress in ash-leaf maple (*Acer negundo*) and sycamore maple (*Acer pseudoplatanus*) species.

2. Material and Method

The study was carried out in the plastic-covered greenhouse of the Düzce University Faculty of Forestry. 3-year-old seedlings were obtained from Ordu Forest Nursery Directorate. For the supplied seedlings to have the same soil type, their existing soils were replaced with the same ratio of peat, perlite, and raw soil mixture. In order to apply UV-B stress only to the plants we want, an aluminum-covered cabin was created inside the greenhouse. UV-B doses were determined as 8 and 12 kJ m-2 h-1, taking into account previous studies. Drought stress was set as weekly irrigation. Control groups (Control, UVB1, UVB2) were watered twice a week; moderately drought applications (moderate drought, moderate drought +UVB1, moderate drought +UVB2) were watered once a week; severe (severe) drought applications (severe drought, severe drought+UVB1, Severe drought+UVB2) were irrigated once every two weeks. In irrigation applications, the seedlings were watered until they reached field capacity.

This study was carried out by establishing 9 trials, such as Control (A1), Moderate Drought (A2), Severe Drought (A3), UVB1 (8 kJ m-2 h-1) (A4), UVB2 (12 kJ m-2 h-1) (A5), Moderate drought+ UVB1 (A2+A4), Moderate Drought+ UVB2 (A2+A5), Severe Drought+ UVB1 (A3+A4), Severe Drought+ UVB2 (A3+A5).

The stoma characters (stoma length, stoma width, stoma pore opening, stoma pore opening width) and stoma number of ash-leaved maple and sycamore maple species were measured. Obtained data were evaluated with the help of the SPSS package program with analysis of variance (ANOVA) and the Duncan test.

3. Result

The effects of drought and UV-B stress on stomata numbers of ash-leaved maple and sycamore maple are shown in Table 1. According to the analysis of variance results, it was determined that there was a statistical difference in the variation of the number of stomata between species ($p<0.05$). When the changes in the number of stomata between the applications were examined, it was determined that there was a significant difference at the 99.9% confidence level in the ash-leaved maple species and at least 95% confidence level in the sycamore maple species. According to the Duncan test result, it can be said that the variation in the number of stomata between species is in the form of ash-leaved maple > sycamore maple.

According to Duncan test results, when the variation in the number of stomata was examined between the applications, it was observed that the lowest stomata number in the ash-leaved maple species was in the severe drought applied (A3) application group, and the highest stomata number was in the high-dose UV-B applied (A5) application group. In the ash-leaved maple species, it is seen that the number of stomata is higher in the application groups that are generally moderately drought-treated. However, the number of stomata in the severe drought and high-dose UV-B applied group (A3+A5) was also higher than the control group (A1). In this application, the number of stomata is thought to increase due to the high dose of UV-B.

When the number of stomata of sycamore maple was examined, it was seen that the lowest number of stomata was in the A3+A5 application group, and the highest stomata number was in the low-dose UV-B applied (A4) application group. It was seen that the number of stomata in sycamore maple species generally decreases with the effect of drought and UV-B. When the two species were compared, it was seen that the number of stomata increased in the application groups with simultaneous drought and UV-B effect in the ash-leaved maple species. At the same time, this situation decreased in the application groups that were simultaneously drought and UV-B applied in the sycamore maple species. The physiological structure of the species may cause this situation. This situation needs to be examined in more detail.

Table 1. Number of stoma changes by species and treatment

Application	Ash-leaved maple (number/mm^2)	Sycamore maple (number/mm^2)	F-value	Average
A1	82.67 ± 6.11 bB	34.67 ± 8.32 cdA	64.800**	51.36 b
A2	117.33 ± 12.85 eB	21.33 ± 6.11 abcA	136.421***	76.92 f
A3	61.33 ± 2.3 aB	30.67 ± 6.11 bcdA	66.125**	38.33 a

Application	Ash-leaved maple (number/mm^2)	Sycamore maple (number/mm^2)	F-value	Average
A4	106.67 ± 6.11 deB	38.67 ± 8.32 dA	130.050***	66.43 de
A5	129.33 ± 6.11 fB	34.67 ± 8.32 cdA	144.029***	81.99 f
A2+A4	97.33 ± 6.11 cdB	36.00 ± 12.22 cdA	75.571**	60.58 cd
A2+A5	109.33 ± 6.11 deB	28.00 ± 4.00 abcdA	372.100***	59.56 e
A3+A4	92.00 ± 4.0 bcB	17.33 ± 6.11 abA	280.900***	59.02 c
A3+A5	104.00 ± 4.0 dB	13.33 ± 2.30 aA	1156.000***	70.27 e
F-value	27.524***	3.858**		30.469***
Average	99.99 B	28.29 A	3197.973***	

In the table, the columns show the differences between applications, and the rows show the differences between types. According to the Duncan test, a, b, etc., application lettering indicates statistical differences between species. Statistically, *** p<0.001 and ** p<0.01, is significant at the confidence level.

The effects of drought and UV-B stress on stomata lenght of ash-leaved maple and sycamore maple are shown in Table 2. According to the results of ANOVA, it was determined that there were significant differences in stomatal length change between species ($p \leq 0.05$). It was determined that there was a significant difference of 99.9% confidence level in the ash-leaved maple species and at least 95% confidence level statistically between the applications in the sycamore maple species ($p > 0.05$).

According to Duncan test results, when the variation of stomatal length between applications is examined, it is seen that the lowest stomatal length in the A3+A5 application group and the highest stomatal length in the application groups (drought stress not applied) (A1, A4, and A5) in the ash-leaved maple. In general, the stomatal length of the ash-leaved maple species decreases with the effect of drought.

When we examine the stomata size data of sycamore maple, it is seen that the lowest stomatal length was in the control (A1) application group and the highest stomatal length was in the severe drought and low-dose UV-B applied group (A3+A4). Generally, stomatal length in sycamore maple tree species increases with moderate drought and UV-B effect. However, it was observed at the lowest level in both severe drought and high-dose UV-B applied (A3+A5) application group. When we compare the two species, the stomata size is generally higher in sycamore maple.

Table 2. Variation of stoma length (μm) by species and application

Application	Ash-leaved maple (μm)	Sycamore maple (μm)	F-value	Average
A1	13.18 ± 2.53 dA	15.03 ± 1.80 aB	22.045***	13.97 de
A2	12.90 ± 2.13 cdA	17.02 ± 3.31 bcB	41.816***	13.53 cde
A3	12.25 ± 1.84 bcA	15.43 ± 2.93 abB	30.490***	13.31 bcd
A4	13.49 ± 2.11 dA	16.43 ± 2.29 abcB	39.001***	14.27 e
A5	13.49 ± 2.75 dA	17.06 ± 2.05 bcB	37.698***	14.25 e
A2+A4	12.90 ± 2.79 bcA	16.71 ± 2.28 abcB	53.840***	13.48 bcde
A2+A5	11.86 ± 1.93 abA	16.98 ± 2.19 bcB	111.147***	12.90 bc
A3+A4	11.49 ± 2.20 abA	17.36 ± 2.81 cB	82.603***	12.60 b
A3+A5	11.28 ± 2.58 aA	15.26 ± 1.85 abB	22.092***	11.74 a
F-value	9.857***	2.331*		7.855***
Average	12.53 A	16.36 B	383.034***	

In the table, the columns show the differences between applications, and the rows show the differences between types. According to the Duncan test, a, b, etc., application lettering indicates statistical differences between species. Statistically, *** p<0.001 and ** p<0.01, is significant at the confidence level.

The effects of drought and UV-B stress on the stomatal width of ash-leaved maple and sycamore maple are shown in Table 3. According to the ANOVA results, it was determined that there was no significant difference ($p > 0.05$) in the variation of stomatal width between species in A3+A5 and A3 applications, while there was a significant difference ($p \leq 0.05$) in other applications. It was determined that there were significant differences at the 99.9% confidence level between the treatments in both species in stomatal width change ($p < 0.001$). In general, the stomatal width is ash-leaved maple <sycamore maple.

According to Duncan's test results, it is seen that the lowest stomatal width in the A1 application group and the highest stomatal width in the mild drought and low-dose UV-B applied (A2+A4) application group in the ash-leaved maple species. The stomatal width increases due to stress in the ash-leaved maple species. It is seen that the most significant increase in stomatal width is observed only in the application of high-dose UV-B (A5).

In the sycamore maple species, it is seen that the lowest stomatal width was in the low-dose UV-B applied (A4) application group, and the highest stomatal width was in the A2+A4 application group. The stomatal width in the sycamore maple

species is generally higher in the application groups exposed to moderate drought, and UV-B stresses simultaneously. It was determined to be high only in the A5 application, even though it was exposed to a single stress.

Table 3. Variation of stomatal width (μm) by species and application

Application	Ash-leaved maple (number/mm^2)	Sycamore maple (number/mm^2)	F-value	Average
A1	11.37 ± 2.07 aA	12.88 ± 2.07 abcB	19.947***	12.04 a
A2	12.15 ± 1.19 bcA	12.90 ± 1.71 abcB	4.610*	12.27 ab
A3	12.10 ± 1.66 bcB	11.85 ± 3.56 ab	0.152 ns	12.01 a
A4	12.52 ± 1.28 cdB	11.24 ± 3.30 aA	8.609**	12.18 ab
A5	12.74 ± 1.63 dA	14.36 ± 2.74 cB	14.568***	13.08 cd
A2+A4	13.29 ± 1.66 eA	14.42 ± 3.16 cB	5.365*	13.60 d
A2+A5	11.95 ± 1.49 bA	14.16 ± 1.96 cB	31.818***	12.40 ab
A3+A4	12.49 ± 1.39 cdA	13.61 ± 3.32 bcB	4.504*	12.70 bc
A3+A5	12.62 ± 1.25 cd	12.52 ± 1.64 abc	0.062 ns	12.61 abc
F-value	9.059***	4.012***		6.955***
Average	12.35 A	13.10 B	25.042***	

In the table, the columns show the differences between applications, and the rows show the differences between types. According to the Duncan test, a, b, etc., application lettering indicates statistical differences between species. Statistically, *** $p<0.001$ and ** $p<0.01$, is significant at the confidence level.

The effects of drought and UV-B stress on the stomatal pore size of ash-leaved maple and sycamore maple are shown in Table 4. According to the ANOVA results, there were significant differences in the variation of stomatal pore size between species ($p\leq0.05$). It was determined that there was a significant difference of at least 95% confidence level in both species in the variation of stoma pore size between applications.

According to the table values, it is seen that the smallest stoma pore size is in the A3+A4 and A3+A5 application groups, while the largest stomatal pore size is in the A1, A2, A4, and A5 application groups. It can say that stoma pore size decreases in ash-leaved maple species with severe drought and UV-B effect.

Generally, the variation in stomatal pore size between species is seen as ash-leaved maple <sycamore maple. In the sycamore maple species, the smallest stoma pore size is seen in the A3+A5 application, and the largest stoma pore size is in the A2 application. The stoma pore size of sycamore maple species decreases with severe drought and high dose UV-B effect. Both species' smallest stomatal pore size was observed in the treatment groups with severe drought + UV-B application.

Table 4. Variation of stoma pore size (μm) by species and application

Application	Ash-leaved maple (number/mm^2)	Sycamore maple (number/mm^2)	F-value	Average
A1	7.16 ± 1.71 eA	8.49 ± 1.52 abB	25.134***	7.76 b
A2	7.24 ± 1.32 eA	10.57 ± 2.61 cB	59.897***	7.75 b
A3	6.68 ± 1.22 cdA	8.75 ± 1.95 abB	29.174***	7.37 b
A4	7.03 ± 1.25 deA	9.00 ± 2.40 abB	30.660***	7.55 b
A5	7.43 ± 1.49 eA	9.13 ± 1.34 abcB	27.529***	7.79 b
A2+A4	6.50 ± 1.54 cA	9.65 ± 1.86 bcB	73.409***	7.35 b
A2+A5	6.28 ± 1.11 bA	10.56 ± 2.38 cB	143.340***	7.15 b
A3+A4	5.74 ± 1.37 aA	9.69 ± 2.53 bcB	74.719***	6.48 a
A3+A5	5.97 ± 1.31 abA	7.92 ± 1.56 aB	18.720***	6.19 a
F-value	14.485***	3.079**		8.102***
Average	6.67 A	9.30	400.432***	

In the table, the columns show the differences between applications, and the rows show the differences between types. According to the Duncan test, a, b, etc., application lettering indicates statistical differences between species. Statistically, *** $p<0.001$ and ** $p<0.01$, is significant at the confidence level.

The effects of drought and UV-B stress on the stomatal pore of ash-leaved maple and sycamore maple are shown in Table 5. According to the ANOVA results, there was a significant difference at a 99.9% confidence level in both tree species in the variation of stoma pore width between applications ($p<0.001$). In sycamore maple species, it was determined to be significant with at least a 95% confidence level. It was determined that the variation of stoma pore width based on species was not a statistically significant difference, only in A4 and A3+ A4 applications ($p>0.05$). All other applications had a significantly differed of at least 95% confidence level.

According to Duncan's test results, it is seen that the smallest stomatal pore size in the A3+A5 application group and the largest pore size in the A1 application group in the ash-leaved maple species. In general, it was observed that the stomatal pore of the ash-leaved maple tree species was negatively affected by the application groups that were exposed to UV-B radiation with severe drought.

In the sycamore maple tree species, it is seen that the lowest stomatal pore width is in the A4 and A5 application groups, where only UV-B is applied, and the highest stomatal pore width is in the moderate drought (A2) application group. The stoma pore size of sycamore maple species is adversely affected by high-dose UV-B.

Table 5. Variation of stoma pore size (μm) by species and application

Application	Ash-leaved maple (number/mm^2)	Sycamore maple (number/mm^2)	F-value	Average
A1	4.11 ± 1.77 eB	2.31 ± 0.44 abA	24.105***	3.59 def
A2	3.84 ± 0.64 deB	2.94 ± 0.69 cA	25.944***	3.70 f
A3	3.84 ± 0.84 deB	2.20 ± 0.59 abA	69.574***	3.29 cd
A4	3.75 ± 0.72 dB	2.09 ± 0.57 aA	121.474***	3.31 cde
A5	4.06 ± 0.89 deB	1.93 ± 0.51 aA	133.490***	3.61 df
A2+A4	3.35 ± 0.55 cB	2.35 ± 0.61 abA	60.100***	3.08 bc
A2+A5	3.10 ± 0.80 bcB	2.29 ± 0.41 abA	19.523***	2.94 ab
A3+A4	2.84 ± 0.65 abB	2.22 ± 0.72 abA	11.288**	2.72 a
A3+A5	2.65 ± 0.65 aB	2.57 ± 0.67 bc	0.159 ns	2.64 a
F-value	28.028***	4.536***		14.318***
Average	3.50 B	2.32 A	254.349***	

In the table, the columns show the differences between applications, and the rows show the differences between types. According to the Duncan test, a, b, etc., application lettering indicates statistical differences between species. Statistically, *** $p<0.001$ and ** $p<0.01$, is significant at the confidence level.

4. Discussion

As a result of the study, it was determined that the UV-B intensity directly affected the number of stomata in general, and the number of stomata increased as the UV-B intensity increased. It was determined that the number of stomata decreased with the effect of severe drought in the ash-leaved maple species. In this case, it was observed that the number of stomata in the sycamore maple species did not decrease much with the effect of severe drought. However, there was a serious decrease in stomata number when exposed to high-dose UV-B with severe drought.

Studies show that the number of stomata is significantly affected by drought. [24], stated that the number of stomata in limited irrigation applications is higher than in control. [25] stated that stomatal density first decreases and then increases in water deficiency. [26], stated that the stomatal density of *Zinnia elegans* plant increased by 50% (moderate under-irrigation) irrigation and 25% (severe under-irrigation) irrigation. They also found that stomatal size decreased at 25% irrigation.

As a result of the study, it was determined that the number of stomata increased as the UV-B intensity and drought severity increased in the ash-leaved maple species. In this case, it is thought that the ash-leaved maple, which is exposed to UV-B and drought stress, increases the number of stomata. Therefore, it can be interpreted that the change in the number of stomata is generally directly proportional to UV-B and drought severity. However, it was observed that the number of stomata in individuals exposed to severe drought and UV-B radiation in the sycamore maple species decreased. It was determined that sycamore maple increased to a certain severity of drought and UV-B severity but decreased simultaneously with the effect of severe drought and UV-B. Although it was observed that the change in the number of stomata changes depending on the application, the reactions of increasing and decreasing the number of stomata were different in different species exposed to the same applications. [27] stated that the density of axial stomata in *Wedelia chinensis* (Osbeck) Merr. plant, which was exposed to UV-B radiation, increased. Some studies have stated that the decrease in the water supply in the soil increases the stomatal density [28].

In the ash-leaved maple species, drought was observed to increase the stomatal length in general. On the other hand, [26] found that the size of the stomata in *Zinnia elegans* plant decreased in severely deficient irrigation. However, the study determined that the stomatal length was lower in individuals exposed to drought and high-dose UV-B than in the control group. In general, UV-B intensity directly affects the stomatal length, and low doses of UV-B increase the stomatal length. However, as the intensity of UV-B radiation increases, the stomatal length decreases. Therefore, stomatal length is thought to be directly proportional to drought severity and inversely proportional to UV-B radiation intensity. It can be said that stoma width and pore sizes generally vary depending on the species. Previous studies show that stomatal movements are

controlled by ethylene, but this needs to be more consistent in the stomatal effect [29-31]. Many studies on stomata have explained UV-B radiation in detail [20], [32].

The results show drought stress is generally more effective on stomatal characters than UV-B stress. Different results have been obtained in studies on this subject. [1], suggested that exposure to UV-B radiation may partially reduce drought stress due to changes in wax deposition or epidermal anatomy. [33], in their study on *C. paliurus*, found that as the drought increased, the stomatal opening decreased. [34] found that drought stress caused a slight increase in the width and length of the stomatal opening in *V. underground* L. Verdc.

As it becomes more intense depending on the intensity of drought stress, it is seen that the thickness of the upper and lower epidermis of the leaf decreases significantly. However, the upper and lower cuticle thickness increases significantly [25] under water deficit conditions, stomatal length, and both upper and lower cuticles of flag leaves. They stated that the area of their surfaces decreased, but it did not affect the stomatal density and width on both surfaces [35]. [28] also stated that the decrease in water supply increases the stomatal density and decreases the leaf area. [33] stated that there are significant differences in stomatal width, stomatal opening, and stomatal density of *C. paliurus* under the influence of drought.

The effects of global climate change are still largely uncertain [36-37]. [38] highlight uncertainties regarding the future terrestrial carbon cycle and the need to understand stomatal behavior during drought better. [39] examined the effect of UV-B radiation on *Pinus pinea* L. and *Pinus halepensis* and stated that UV-B radiation might benefit Mediterranean pines by partially mitigating the adverse effects of summer drought. [40] noted that drought significantly reduced leaf area in *Rosmarinus officinalis* L., *Olea europea* L., and *Lavandula stoechas* species and that exposure of plants to high UV-B radiation before and during drought stress had no significant effect on plant growth or photosynthetic activities. On the other hand, [41] stated that drought and UV-B radiation have a combined effect on photosynthetic gas exchange.

When the studies are examined, it is seen that the effects of UV-B stress and drought stress on plant stomatal characters remain unclear. It is necessary to examine in detail whether this situation changes depending on the species or according to the application. Plant phenotypic characters are shaped by the interaction of genetic structure [42-44] and environmental conditions [13], [45-47]. Stomatal characters are also significantly affected by environmental factors as well as genetic structure. In addition to changes in atmospheric conditions [48-50], changes in edaphic factors such as soil moisture and nutrient status were found to change stomatal morphology [51]. Plant stomata, the vital gateway between atmosphere and plant, may have a central role in vegetation/plant responses to environmental situations investigated at the ecosystem and global levels, as well as from molecular and whole plant perspectives [52].

5. Conclusion and Suggestion

The study results generally show that UV-B stress is more effective on stomatal characters than drought stress. However, the combined effect of drought and UV-B increase on plants, which is predicted to increase due to global climate change, remains unclear. It remains unclear whether the opposite reactions of different species to the same applications in the species subject to the study are due to the structure of the species or whether it is due to the difference in the responses given to the applications. Therefore, it is recommended that studies on the subject be continued by diversifying and increasing.

In conclusion, it was observed that the stomatal behavior of ash-leaved maple was less affected by UV-B and drought stress than sycamore maple species. It could be said that the ash-leaved maple is more resistant to drought and UV-B stress than the sycamore maple. In this case, it may be more appropriate to prefer ash-leaved trees in urban afforestation, where drought and UV-B effects are felt the most, today, where the pace of global climate change is kept up.

It is thought that more successful afforestation areas will be created for ash-leaved maple compared to sycamore maple in forest afforestation studies. Therefore, it may be preferred in such fields.

Competing Interest / Conflict of Interest

All authors certify that they have no affiliations with or involvement in any organization or entity with any financial interest or non-financial interest in the subject matter or materials discussed in this manuscript.

Author Contribution

Hatice Çobanoğlu: Conceptualization, Methodology, Software, Data curation, Writing- Original draft preparation; Visualization, Investigation. Şemsettin Kulaç: Data curation, Writing- Original draft preparation. Hakan Şevik: Software, Validation, Writing- Reviewing and Editing.

Acknowledgements

This paper is part of Hatice Çobanoğlu's dissertation in the doctoral thesis, thesis titled "The Effect of Drought and UV-B Stress on Some Anatomical and Morphological Characters in *Acer negundo* L. and *Acer pseudoplatanus* L. Species". Department of Forest Engineering, Faculty of Forestry, Düzce University.

It is also a part of the TÜBİTAK project 222O792 titled "The Effect of Drought and Uv-B Stress on Some Micromorphological Characters in *Acer Negundo* and *Acer Pseudoplatanus* Species".

Thank Tubitak and YOK 100/2000 Scholarship.

5. References

[1] Gitz, D. C., Liu-Gitz, L., Britz, S. J., & Sullivan, J. H. (2005). Ultraviolet-B effects on stomatal density, water-use efficiency, and stable carbon isotope discrimination in four glasshouse-grown soybean (Glyicine max) cultivars. Environmental and Experimental Botany, 53(3), 343-355.

[2] Hectors, K., Prinsen, E., De Coen, W., Jansen, M. A., & Guisez, Y. (2007). *Arabidopsis thaliana* plants acclimated to low dose rates of ultraviolet B radiation show specific changes in morphology and gene expression in the absence of stress symptoms. New Phytologist, 175(2), 255-270.

[3] Liang, T., Shi, C., Peng, Y., Tan, H., Xin, P., Yang, Y., ... & Liu, H. (2020). Brassinosteroid-activated BRI1-EMS-SUPPRESSOR 1 inhibits flavonoid biosynthesis and coordinates growth and UV-B stress responses in plants. Plant Cell, 32(10), 3224-3239.

[4] Booij-James, I.S., Dube, S.K., Jansen, M.A., Edelman, M., & Mattoo, A.K. (2000). Ultraviyole-B radyasyonu, fenolik metabolizmada değiştirilmiş Arabidopsis mutantlarında fotosistem II reaksiyon merkezi heterodimerinin ışık aracılı cirosunu etkiler. Bitki Fizyolojisi, 124(3), 1275-1284.

[5] Işınkaralar, K., & Erdem, R. (2021). Changes of calcium content on some trees in Kocaeli. Kastamonu University Journal of Engineering and Sciences, 7(2), 148-154.

[6] Teramura, A. H., & Sullivan, J. H. (1994). Effects of UV-B radiation on photosynthesis and growth of terrestrial plants. Photosynthesis Research, 39, 463-473.

[7] Sevik, H., Isinkaralar, K., & Isinkaralar, O. (2018). Indoor air quality in hospitals: the case of Kastamonu Turkey. J Chem Biol Phys Sci Sect D, 9(1), 67-73.

[8] Varol, T., Cetin, M., Ozel, H.B., Sevik, H., & Zeren Cetin, I. (2022b). The effects of climate change scenarios on *Carpinus betulus* and *Carpinus orientalis* in Europe. Water, Air, & Soil Pollution, 233(2), 45.

[9] Isinkaralar, O. (2023). Bioclimatic comfort in urban planning and modeling spatial change during 2020–2100 according to climate change scenarios in Kocaeli, Türkiye. International Journal of Environmental Science and Technology, 20(7), 7775–7786.

[10] Yayla, E. E., Sevik, H., & Isinkaralar, K. (2022). Detection of landscape species as a low-cost biomonitoring study: Cr, Mn, and Zn pollution in an urban air quality. Environmental Monitoring and Assessment, 194(10), 1-10.

[11] Isinkaralar, O., & Varol, C. (2023). A cellular automata-based approach for spatio-temporal modeling of the city center as a complex system: The case of Kastamonu, Türkiye. Cities, 132, 104073.

[12] Cetin, M., Sevik, H., Koc, I., & Cetin, I. Z. (2023). The change in biocomfort zones in the area of Muğla province in near future due to the global climate change scenarios. Journal of Thermal Biology, 112, 103434.

[13] Cobanoglu, H., Sevik, H., Koç, İ. (2023). Do Annual Rings Really Reveal Cd, Ni, and Zn Pollution in the Air Related to Traffic Density? An Example of the Cedar Tree. Water, Air, & Soil Pollution, 234(2), 65.

[14] Isinkaralar, O., Varol, C., & Yilmaz, D. (2022). Digital mapping and predicting the urban growth: integrating scenarios into cellular automata—Markov chain modeling. Applied Geomatics, 1-11.

[15] Çobanoğlu, H., & Kulaç, Ş. (2023). Effect of Drought and UV-B Stress on Leaf Morphology of Ash-Leaved Maple and Sycamore Maple, Turkish Journal of Agriculture - Food Science and Technology, (InPress).

[16] Isinkaralar, K., & Erdem, R. (2021). Landscape plants as biomonitors for magnesium concentration in some species. International Journal of Progressive Sciences and Technologies, 29(2), 468-473.

[17] Isinkaralar, K. (2022). Temporal variability of trace metal evidence in Cupressus arizonica, Platanus orientalis, and Robinia pseudoacacia as pollution-resistant species at an industrial site. Water, Air, and Soil Pollution, 233(7), 250.

[18] Koç, İ., & Nzokou, P. (2023). Combined effects of water stress and fertilization on the morphology and gas exchange parameters of 3-year-old *Abies fraseri* (Pursh) Poir. Acta Physiologiae Plantarum, 45(3), 49.

[19] Yigit, N., Mutevelli, Z., Sevik, H., Onat, S.M., Ozel, H.B., Cetin, M., & Olgun, C. (2021). Identification of some fiber characteristics in *Rosa* sp. and *Nerium oleander* L. wood grown under different ecological conditions. BioResources, 16(3), 5862-5874. https://doi.org/10.15376/biores.14.3.7015-7024

[20] Isinkaralar, K. (2022). Some atmospheric trace metals deposition in selected trees as a possible biomonitor. Romanian Biotechnological Letters, 27(1), 3227-3236.
[21] Koç, İ., & Nzokou, P. (2022b). Do various conifers respond differently to water stress. A comparative study of white pine, concolor and balsam fir. Kastamonu University Journal of Forest Faculty, 22(1), 1-16.
[22] Yigit, N. (2019). Determination of heavy metal accumulation in air through annual rings: The case of Malus floribunda species. Applied Ecology and Environmental Research, 17(2), 2755-2764.
[23] Cantürk, U. (2023). Kuraklık ve UV-B streslerinin Türkiye'de yayılış gösteren bazı ıhlamur (*Tilia* sp.) türlerinde fizyolojik ve biyokimyasal değişimler üzerine etkisi. PhD Thesis, Institute of Düzce University Graduate Education Institute. Düzce, Türkiye.
[24] Candar, S., Açıkbaş, B., Korkutal, İ., & Bahar, E. (2021). The effects of water deficit on leaf and stoma morphological properties of wine grapes in thrace region. Ksu Tarim ve Doga Dergisi-Ksu Journal of Agriculture and Nature.
[25] Cao, L., Zhong, Q., Luo, S., Yuan, T., Guo, H., Yan, C., & Yuan, Y. (2018). Variation in leaf structure of Camellia oleifera under drought stress. Forest Research, Beijing, 31(3), 136-143.
[26] Toscano, S., & Romano, D. (2021). Morphological, physiological, and biochemical responses of zinnia to drought stress. Horticulturae, 7(10), 362.
[27] Rai, K., & Agrawal, S. B. (2022). Effects of elevated ultraviolet-B on the floral and leaf characteristics of a medicinal plant *Wedelia chinensis* (Osbeck) Merr. along with essential oil contents. Tropical Ecology, 1-17.
[28] Fraser, L. H., Greenall, A., Carlyle, C., Turkington, R., & Friedman, C. R. (2009). Adaptive phenotypic plasticity of Pseudoroegneria spicata: response of stomatal density, leaf area and biomass to changes in water supply and increased temperature. Annals of Botany, 103(5), 769-775.
[29] Watkins, J. M., Hechler, P. J., & Muday, G. K. (2014). Ethylene-induced flavonol accumulation in guard cells suppresses reactive oxygen species and moderates stomatal aperture. Plant Physiology, 164(4), 1707-1717.
[30] Tanaka, Y., Sano, T., Tamaoki, M., Nakajima, N., Kondo, N., & Hasezawa, S. (2005). Ethylene inhibits abscisic acid-induced stomatal closure in Arabidopsis. Plant physiology, 138(4), 2337-2343.
[31] Tanaka, Y., Sano, T., Tamaoki, M., Nakajima, N., Kondo, N., & Hasezawa, S. (2006). Cytokinin and auxin inhibit abscisic acid-induced stomatal closure by enhancing ethylene production in Arabidopsis. Journal of Experimental Botany, 57(10), 2259-2266.
[32] Yigit, N., Cetin, M., & Sevik, H. (2018). The change in some leaf micromorphological characters of *Prunus laurocerasus* L. species by their habitat. Turkish Journal of Agriculture-Food Science and Technology, 6 (11), 1517-1521.
[33] Li, C., Wan, Y., Shang, X., & Fang, S. (2022). Responses of microstructure, ultrastructure and antioxidant enzyme activity to PEG-induced drought stress in *Cyclocarya paliurus* seedlings. Forests, 13(6), 836.
[34] Fatimah, S., Ariffin, A., Rahmi, A. N., & Kuswanto, K. (2020). Tolerance and determinants of drought character descriptors of the Madurese landrace bambara groundnut (*Vigna subterranea*). Biodiversitas Journal of Biological Diversity, 21(7).
[35] Mehri, N., Fotovat, R., Saba, J., & Jabbari, F. (2009). Variation of stomata dimensions and densities in tolerant and susceptible wheat cultivars under drought stress. Journal of Food Agriculture and Environment, 7(1), 167-170.
[36] Varol, T., Canturk, U., Cetin, M., Ozel, H.B., & Sevik, H. (2021). Impacts of climate change scenarios on European ash tree (*Fraxinus excelsior* L.) in Turkey. Forest Ecology and Management, 491, 119199.
[37] Tekin, O., Cetin, M., Varol, T., Ozel, H. B., Sevik, H., & Zeren Cetin, I. (2022). Altitudinal migration of species of Fir (Abies spp.) in adaptation to climate change. Water, Air, and Soil Pollution, 233(9), 385.
[38] Wankmüller, F. J., & Carminati, A. (2022). Stomatal regulation prevents plants from critical water potentials during drought: Result of a model linking soil–plant hydraulics to abscisic acid dynamics. Ecohydrology, 15(5), e2386.
[39] Petropoulou, Y., Kyparissis, A., Nikolopoulos, D., & Manetas, Y. (1995). Enhanced UV-B radiation alleviates the adverse effects of summer drought in two Mediterranean pines under field conditions. Physiologia Plantarum, 94(1), 37-44.
[40] Nogués, S., & Baker, N. R. (2000). Effects of drought on photosynthesis in Mediterranean plants grown under enhanced UV-B radiation. Journal of Experimental Botany, 51(348), 1309-1317.
[41] Sullivan, J. H., & Teramura, A. H. (1990). Field study of the interaction between solar ultraviolet-B radiation and drought on photosynthesis and growth in soybean. Plant Physiology, 92(1), 141-146.
[42] Isinkaralar, K., Koc, I., Erdem, R., & Sevik, H. (2022). Atmospheric Cd, Cr, and Zn deposition in several landscape plants in Mersin, Türkiye. Water, Air, and Soil Pollution, 233(4), 120.
[43] Erdem, R., Çetin, M., Arıcak, B., & Sevik, H. (2023). The change of the concentrations of boron and sodium in some forest soils depending on plant species. Forestist (InPress).

[44] Kurz, M., Kölz, A., Gorges, J., Carmona, B.P., Brang, P., Vitasse, Y., ... & Csilléry, K. (2023). Tracing the origin of Oriental beech stands across Western Europe and reporting hybridization with European beech–Implications for assisted gene flow. Forest Ecology and Management, 531, 120801.

[45] Savas, D. S., Sevik, H., Isinkaralar, K., Turkyilmaz, A., & Cetin, M. (2021). The potential of using Cedrus atlantica as a biomonitor in the concentrations of Cr and Mn. Environmental Science and Pollution Research, 28(39), 55446-55453.

[46] Karacocuk, T., Sevik, H., Isinkaralar, K., Turkyilmaz, A., & Cetin, M. (2022). The change of Cr and Mn concentrations in selected plants in Samsun city center depending on traffic density. Landscape and Ecological Engineering, 1-9.

[47] Sulhan, O. F., Sevik, H., & Isinkaralar, K. (2023). Assessment of Cr and Zn deposition on Picea pungens Engelm. in urban air of Ankara, Türkiye. Environment, Development and Sustainability, 25(5), 4365-4384.

[48] Bayraktar, E. P., Isinkaralar, O., & Isinkaralar, K. (2022). Usability of several species for monitoring and reducing the heavy metal pollution threatening the public health in urban environment of Ankara. World Journal of Advanced Research and Reviews, 14(3), 276-283.

[49] Işınkaralar, K., Işınkaralar, Ö., & Şevik, H. (2022). Usability of some landscape plants in biomonitoring technique: an anaysis with special regard to heavy metals. Kent Akademisi, 15(3), 1413-1421.

[50] Isinkaralar, K. (2022). The large-scale period of atmospheric trace metal deposition to urban landscape trees as a biomonitor. Biomass Conversion and Biorefinery, 1-10.

[51] Xu, Z., & Zhou, G. (2008). Responses of leaf stomatal density to water status and its relationship with photosynthesis in a grass. Journal of Experimental Botany, 59(12), 3317-3325.

[52] Nilson, S. E., & Assmann, S. M. (2007). The control of transpiration. Insights from Arabidopsis. Plant physiology, 143(1), 19-27.

Kastamonu University
Journal of Engineering and Sciences
e-ISSN 2667-8209
http://dergipark.gov.tr/kastamonujes

Protective Effect of Celeriac (*Apium graveolens*) Leaf Essential Oil on Temperature and Oxygen-Induced Fish Oil Oxidation

Osman Sabri Kesbiç

Department of Animal Nutrition and Nutritional Diseases, Veterinary Faculty of Kastamonu University, 37150, Kastamonu, Türkiye
***Corresponding Author:** okesbic@kastamonu.edu.tr

Received: **May 16, 2023** ◆ Accepted: **June 17, 2023** ◆ Published Online: **June 21, 2023**

Abstract: The purpose of this work was to identify the volatile components of essential oil extracted from Celeriac (*Apium graveolens*) leaves (CEO) and assess its antioxidant performance during the thermal oxidation of fish oil. Steam distillation method and Clevenger apparatus was used to extract of CEO from fresh leafs. The volatile component analysis revealed that 98.81% of the volatile components in the resulting product could be recognized. Following examination, the principal components of the product were discovered to be Phthalide (3-isobutylidene) and Fenipentol with a concentration of 49.42% and 28.45% respectively. The product's antioxidant activity was tested using a 2,2-diphenyl-1-picrylhydrazyl (DPPH) study. The 50% inhibitory concentration value (IC50) for CEO was discovered to be 30.52 ppm by the study. To test the product's ability to protect fish oil from oxidation, CEO ratios of 0% (CEO0), 0.1% (CEO0.1), 0.5% (CEO0.5), 1% (CEO1), and 3% (CEO3) were added to fish oil, and the experimental groups were subjected to 24 hours of oxidation at 70 °C with continuous ventilation. According to the oxidation investigation, the addition of CEO suppressed fish oil oxidation and significantly reduced the product's oxidation radicals ($p<0.05$) depending on the CEO concentration. According to the study's results, the group with 3% CEO had the lowest oxidation of fish oil caused by temperature and oxygen contamination.

Keywords: *Apium graveolens*, Essential oil, Volatile compounds, Natural antioxidant

Öz: Bu çalışmanın amacı, Kereviz (*Apium graveolens*) yapraklarından (CEO) elde edilen uçucu yağın uçucu bileşenlerini tanımlamak ve balık yağının termal oksidasyonu sırasında antioksidan performansını değerlendirmektir. Taze yağraklardan CEO saflaştırılması için buhardistilasyonu metodu ve Clavenger düzeneği kullanılmıştır. Uçucu bileşen analizi, elde edilen üründeki uçucu bileşenlerin %98,81'inin tanınabildiğini ortaya koymuştur. İncelemenin ardından, ürünün ana bileşenlerinin sırasıyla %49,42 ve %28,45 konsantrasyonla Ftalit (3-izobütiliden) ve Fenipentol olduğu tespit edilmiştir. Ürünün antioksidan aktivitesi 2,2-difenil-1-pikrilhidrazil (DPPH) çalışması kullanılarak test edilmiştir. Çalışmada CEO için %50 inhibitör konsantrasyon değeri (IC50) 30.52 ppm olarak bulunmuştur. Ürünün balık yağını oksidasyondan koruma kabiliyetini test etmek için balık yağına %0 (CEO0), %0,1 (CEO0,1), %0,5 (CEO0,5), %1 (CEO1) ve %3 (CEO3) oranlarında CEO eklenmiş ve deney grupları sürekli havalandırma ile 70 °C'de 24 saat oksidasyona tabi tutulmuştur. Oksidasyon araştırmasına göre, CEO ilavesi balık yağı oksidasyonunu baskılamış ve CEO konsantrasyonuna bağlı olarak ürünün oksidasyon radikallerini önemli ölçüde azaltmıştır ($p<0.05$). Çalışmanın sonuçlarına göre, %3 CEO içeren grup, sıcaklık ve oksijen kontaminasyonunun neden olduğu en düşük balık yağı oksidasyonuna sahipti.

Anahtar Kelimeler: *Apium graveolens*, Esansiyel yağ, Uçucu bileşen, Doğal antioksidan

1. Introduction

The exponential growth of the global population is progressively diminishing the probability of individuals accessing high-quality sustenance on a daily basis. Aquaculture, particularly the practice of fish farming, is widely regarded as a highly advantageous alternative due to its potential to offer a resolution to this issue [1]. According to data from 2017, the total fish production amounted to 179 million tons, of which approximately 88% was allocated for human consumption, while the remaining 12% was utilized for non-food purposes. The utilization of fish processing by-products and/or surplus catch, which is estimated to account for 25-35% of the overall fish proportion, is reportedly directed toward the production of fishmeal and fish oil [2]. Fishmeal and fish oil are widely recognized as highly nutritious and easily digestible fundamental sources of protein and lipids in the context of aquaculture [3]. The utilization proportions of fishmeal and fish oil in feed formulations for aquaculture are exhibiting a distinct declining pattern, as per the Food and Agriculture Organization's report of 2022 [4]. The utilization of nutritious and superior feed in fish nutrition is crucial for enhancing the quality of products and promoting sustainable development in the aquaculture sector. The quality of fish feed has a direct correlation with the growth, reproduction, and meat quality of fish. Therefore, in order to ensure sustainable aquaculture, it is imperative to reduce the amount of fish meal and fish oil added to fish feeds and to improve their quality [5, 6].

Fish oil is a secondary product that is derived from the pressing procedure of fish meals. It is obtained through the process of separating and purifying fish and its particles from the press liquid. According to Korkut, et al. [7], the oil content of fish is influenced by various factors such as their feeding habits, species, seawater temperature, and geographical location where they are caught. Fish oil serves as the primary origin of polyunsaturated fatty acids Omega-3 (ω-3) and Omega-6 (ω-6). The presence of polyunsaturated fatty acids (PUFA) in fish oil is known to render it susceptible to swift oxidation, thereby exerting a detrimental impact on its quality during the storage phase. Consumption of such oxidized fish oil can lead to severe health complications [8]. Fish oils are prone to oxidation due to their high content of polyunsaturated fatty acids (PUFA). The formation of unpleasant odor and quality deterioration significantly diminishes the quality of the product, and in advanced stages, can cause a conversion of fish oil from a nutritious substance to a hazardous one [9]. In addition, the existence of specific pigments namely myoglobin and hemoglobin, alongside minute quantities of metallic ions such as iron and copper, renders fish oil more vulnerable to oil oxidation as per the findings of Hsieh and Kinsella [10]. The process of oxidation has the potential to result in adverse consequences, including but not limited to the impairment of vitamins, alteration of color, and depletion of crucial fatty acids. These outcomes can have a detrimental impact on sensory perception and lead to a reduction in nutritional value [9]. The shelf life of fish oil and fish oil-enriched products is notably diminished by the process of oxidation. The presence of oxygen has been observed to cause oxidation of polyunsaturated fatty acids (PUFA) in fish oil. Environmental factors such as enzymes, light, metal ions, and temperature have the potential to induce degradation. The oxidation process causes the breakdown of hydroperoxides, which in turn leads to the loss of nutrients, sourness, and undesirable flavors [11, 12].

Apium graveolens, commonly known as celeriac, is an herbaceous plant that has gained recognition for its culinary and medicinal properties. The leaves of celeriac have been traditionally used in various cuisines and folk medicine. Recent studies have revealed that celeriac leaf essential oil (CEO) possesses a rich composition of volatile compounds with potential antioxidant properties, making it a promising natural antioxidant for lipid protection. The lipid protective activity of CEO can be attributed to its bioactive constituents, including phthalides, phenolic compounds, monoterpenes, and sesquiterpenes. These compounds exhibit diverse mechanisms of action that contribute to their antioxidant efficacy in lipid systems. Phthalides, such as 3-n-butylphthalide, have been reported to effectively inhibit lipid oxidation by scavenging lipid-derived free radicals and chelating pro-oxidative transition metal ions [13]. Phenolic compounds, another important class of constituents in CEO, act as potent antioxidants by donating hydrogen atoms or electrons to neutralize lipid radicals and break the free radical chain reactions. Furthermore, the monoterpenes and sesquiterpenes found in CEO, such as limonene, α-pinene, and β-caryophyllene, contribute to its lipid protective activity through their radical scavenging and metal chelation abilities [14]. These volatile compounds possess lipophilic properties that enable them to effectively interact with lipid substrates, thereby exerting their antioxidant effects directly within the lipid matrix. Moreover, the underlying mechanisms by which CEO protects lipids can be investigated by assessing its impact on key oxidative markers, including reactive oxygen species (ROS) generation, lipid hydroperoxides, and antioxidant enzyme activities. Understanding these mechanisms will provide valuable insights into the mode of action of CEO in lipid protection and contribute to the development of optimized antioxidant strategies [15].

The employment of antioxidants for the purpose of inhibiting oxidation in fish oil and fish oil-fortified commodities is a prevalent technique in the food sector, aimed at prolonging their period of preservation. Nevertheless, studies have indicated that the utilization of artificial antioxidants may result in enduring issues and buildup within the human body. Consequently, an increasing inclination is observed toward the creation of natural substances possessing antioxidant characteristics. Research has indicated that Celeriac (*Apium graveolens*), a plant that is utilized for both culinary and medicinal purposes, displays robust antioxidant characteristics. The primary aim of this research is to explore the potential application of Celeriac Leaf Essential Oil (CEO) in preserving the oxidative stability of fish oil, a crucial lipid source in the aquaculture feed sector.

2. Material and Method

Preparation of Celery Leaves and Essential Oil Extraction

Celeriac leaves to be used in the study were purchased from Kastamonu local market. The leaves were washed with tap water and dried with a clean paper towel before the oil extraction process. After that, the leaves were cut into small pieces with laboratory scissors and placed in a round bottom flask with distilled water (100g 300 mL^{-1}) [16] and subjected to hydrodistillation with Clevenger apparatus. The upper phase of the distillate accumulated in the collector was taken into amber glass vials. Afterward, the collected essential oil was filled with nitrogen gas and stored at -20°C to be used in the analysis and study.

Determination of Volatile Compound of Celeriac Leaves Essential Oil

The essential oil analysis of volatile components was conducted using GC/MS (Shimadzu GCMS QP 2010 ULTRA). In the course of the analysis, a capillary column of the RTX-5MS brand measuring 30 meters in length, 0.25 millimeters in diameter, and 0.25 micrometers in particle size was employed, with helium serving as the carrier gas. The experimental setup involved setting the column oven temperature to 40 °C, the interface temperature to 250°C, the ion source

temperature to 200°C, and the injection temperature to 250°C. The injection volume utilized in the experiment was 1µL, and the split (1/5) method was employed for injection. The analysis involved a temperature regimen that consisted of heating the sample to 40°C for 3 minutes, followed by a gradual increase from 40°C to 240°C at a rate of 4°C per minute, holding the temperature at 240°C for 10 minutes, and then increasing the temperature from 240°C to 260°C at a rate of 4°C per minute, holding the temperature at 260°C for 10 minutes. The entire oven program lasted for a total of 78 minutes. The determined peaks were subjected to comparison with the W9N11 library, resulting in the identification of volatile compounds [17].

Evaluation of Essential Oil's Antioxidant Activity

The combination of 0.2 mL essential oil, 0.5 mL DPPH solution, and 4 mL 80% ethanol was combined in a 15" vortex and left at room temperature for 15 minutes to assess the scavenging action of the produced essential oil on DPPH radical. The combination was read in a UV-VIS spectrophotometer at 517 nm at the conclusion of the experiment. Absorbances were recorded, and values for the percentage scavenging effect were calculated using the equation below [18]. The same process was done using antioxidants derived from industrial Vitamin-C and antioxidant activity was compared in this manner.

% scavenging activity= [1- (AS/A0)] x100.

The study of Thermal Oxidation

The aim of the study was to investigate the potential protective effect of celery leaf essential oil against the thermal oxidation of fish oil. The experimental design involved the addition of the essential oil to the fish oil at varying ratios of 0% (CEO0), 0.1% (CEO0.1), 0.5% (CEO0.5), 1% (CEO1), and 3% (CEO3), resulting in the formation of distinct experimental groups. The experimental groups were subjected to thermal oxidation at a constant temperature of 70±0.5 °C for a duration of 24 hours while being placed in heat-resistant bottles and provided with continuous ventilation.

Determination of Peroxide Value

The peroxide determination method (Cd 8b-90) published by the American Oil Chemistry Society AOCS [19] was used to determine the effect of thermal oxidation and the preservation of celery leaf essential oil. For this purpose, fish oil without thermal oxidation (Control) and samples taken from the experimental groups were dissolved with g 5 mL^{-1} chloroform, 15 mL acetic acid and 1 mL saturated potassium iodide were added and kept in the dark for 10 min at room temperature. After waiting, it was subjected to titration with 75 mL deionized water and 0.01 N adjusted sodium thiosulfate in the presence of a few drops of starch (1%) indicator. The amount of consumption obtained at the endpoint of the titration, which is the clear color formation, was calculated using the following formula and the peroxide value was calculated.

Peroxide value (PV)= [(V1-V0) x N] / M

V1 and V0 are the amounts spent for the sample and blind respectively, N is the normality of the titration solution and M is the sample weight. The results of the PV analysis performed in three replicates were calculated as meqO_2 kg^{-1} oil.

Statistical Analysis

The data obtained from the experiment were subjected to statistical analysis using the MiniTab software. The data underwent One-way analysis of variance (ANOVA) and was subsequently subjected to the Tukey multiple comparison test. Statistical significance was determined for intergroup differences at a significance level of $p<0.05$.

3. Result

Table 1 displays the profile of the volatile components found in the CEO. The findings indicate that a significant proportion of 98.81% of the volatile component content of the extract was identifiable. The primary constituents of this composition are Phthalide (49.42%), Fenipentol (28.45%), and D-Limonene (6.54%).

Table 1. Volatile profile of Celeriac leaf essential oil (CEO).

Sn	Compound	Retention Time (min.)	Concentration (%)
1	D-Limonene	12.660	6.54
2	1-Propanone,1-(2,4-dimethylphenyl)	34.413	4.04
3	Valeric acid	35.344	4.31

4	Fenipentol	36.442	28.45
5	Phthalide	36.622	49.42
6	3 n butyl phthalide	36.815	6.05
		TOTAL	**98.81**

The study found a correlation between the concentrations of CEO and Vit-C samples in DPPH solution and their respective inhibition percentages, as indicated by correlation factors. A linear relationship was observed between the aforementioned variables. The IC50 values were calculated using the linear equations provided, and the resultant data is illustrated in Figure 1. As demonstrated in Figure 1, the IC50 values for CEO and Vit-C were determined to be 30.52 and 29.93 ppm, respectively.

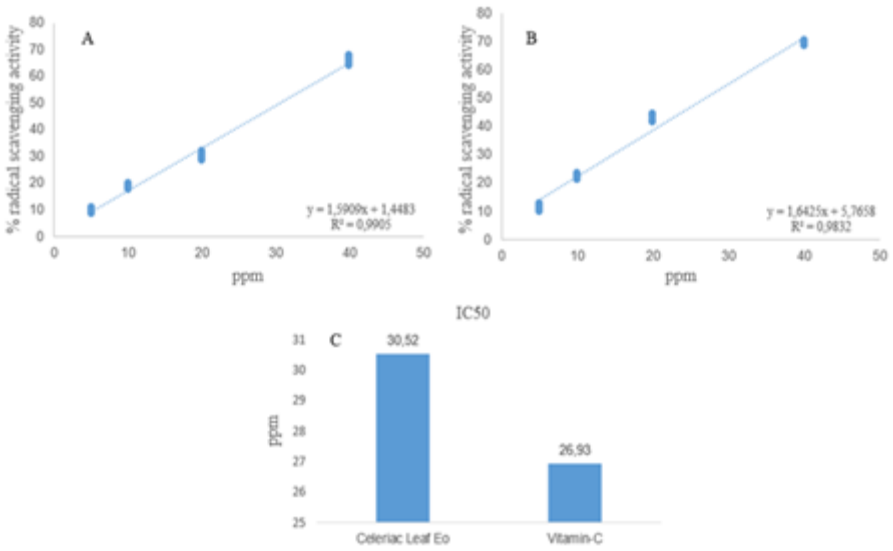

Figure 1. % radical scavenging activity of CEO (A), % radical scavenging activity of Vitamin-C (B) and the minimal concentration of CEO and Vitamin C for 50% radical scavenging (C).

The PV of fish oils subjected to thermal treatment, with varying ratios of CEO addition, as well as fish oil without any addition and thermal oxidation (Control), is depicted in Figure 2.

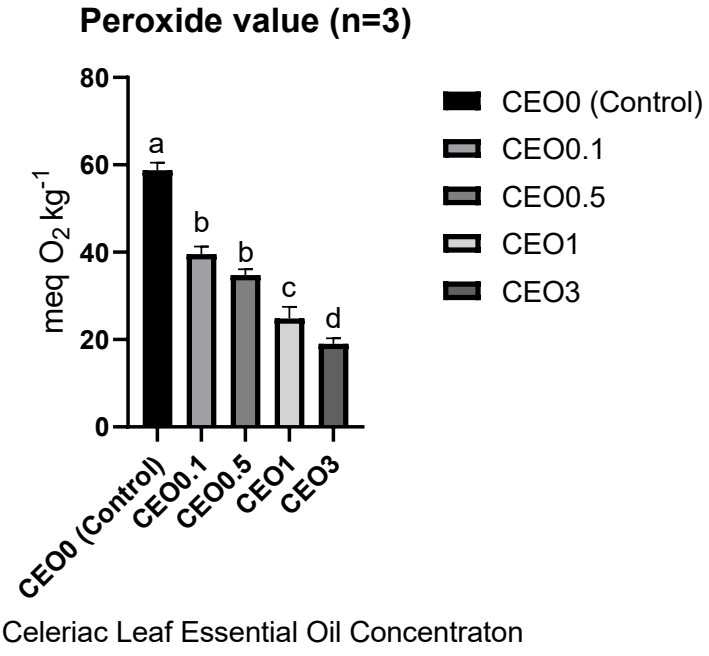

Figure 2. Peroxide values of fish oils containing different ratios of CEO after thermal oxidation

4. Discussion and Conclusion

Essential oils are highly concentrated plant extracts that are widely used in aromatherapy, cosmetics, and as natural remedies for various ailments. They are known for their pleasant aroma and many beneficial properties, including antioxidant and antimicrobial effects [20-22]. One potential application of essential oils is in protecting oil sources from oxidation [23]. Oxidation is a natural process that occurs when oils are exposed to air and light, causing them to break down and lose their nutritional value [24]. This can lead to rancidity, which not only affects the taste and smell of the oil but also reduces its health benefits [25]. Research has shown that certain essential oils, such as oregano, rosemary, and thyme, have strong antioxidant properties that can help protect oils from oxidation. These oils contain compounds such as carvacrol, thymol, and rosmarinic acid, which have been shown to inhibit the oxidation process and prevent the formation of harmful free radicals [26]. While the use of essential oils to protect oil sources from oxidation shows promise, more research is needed to fully understand their effectiveness and determine the optimal conditions for their use. It is also important to note that some essential oils may have adverse effects on certain individuals, so caution should be taken when using them [27]. Overall, the use of essential oils as natural preservatives for oil sources is an intriguing area of research that has the potential to provide a more sustainable and healthful alternative to synthetic preservatives.

Numerous research endeavors have been undertaken to explore the safeguarding properties of plant-based sources on marine oils derived from diverse origins [28-30]. The majority of the conducted studies employed PV as a metric to assess the safeguarding potential of botanical commodities on marine lipid sources. PV is considered to be a highly dependable indicator for identifying the onset of primary oxidation in oils [31]. Oil sources derived from marine organisms, such as fish oil, possess a high concentration of polyunsaturated fatty acids (PUFAs), rendering them vulnerable to oxidative degradation under various environmental stressors, including elevated temperature, light exposure, and humidity. As per good manufacturing practice (GMP), natural antioxidants like vitamin C are incorporated into fish oils produced for feed or food quality, owing to their reported benefits [32]. The present study involved a comparison between the CEO antioxidant activity and vitamin C.

Celeriac (*Apium graveolens*) is a biennial plant belonging to the Apiaceae family, which is widely used as a food and medicinal herb in many countries [33]. Celeriac leaf essential oil is a volatile oil obtained by steam distillation of the leaves of the celeriac plant. CEO is rich in many bioactive compounds, including phenolic compounds, terpenes, and flavonoids, which have been reported to have strong antioxidant activity [34]. As in previous studies, phthalide isomers and numerous bioactive molecules responsible for the distinctive aroma of CEO were identified in the present study. Antioxidants are compounds that protect cells from oxidative stress caused by free radicals, which are highly reactive molecules that can damage cellular components and contribute to the development of many chronic diseases such as cancer, diabetes, and cardiovascular disease. Antioxidants can neutralize free radicals and prevent oxidative damage, thereby protecting cells and tissues from damage [35]. The efficacy of natural antioxidants has been established in various studies [36, 37] like the present study, indicating their potential benefits not only for metabolic processes but also for safeguarding fats against rancidity.

To conclude, it has been demonstrated that the CEO exhibits potent antioxidant properties owing to its elevated levels of bioactive constituents. The potential natural antioxidant properties of CEO render it a promising candidate for employment in the food and feed industries.

Competing Interest / Conflict of Interest

The authors declare that they have no competing interests.

Author Contribution

We declare that all Authors equally contribute.

5. References

[1] Gjedrem, T., Robinson, N., & Rye, M. (2012). The importance of selective breeding in aquaculture to meet future demands for animal protein: a review. Aquaculture, 350, 117-129.
[2] Cashion, T., Le Manach, F., Zeller, D., & Pauly, D. (2017). Most fish destined for fishmeal production are food-grade fish. Fish and Fisheries, 18(5), 837-844.
[3] Jackson, A. J. (2006). The importance of fishmeal and fish oil in aquaculture diets. International Aquafeed, 9(6), 18-21.
[4] Fisheries, F. A. O. (2022). Aquaculture Division. Rome: Food and Agriculture Organization of the United Nations.
[5] Tacon, A. G. (2004). Use of fish meal and fish oil in aquaculture: a global perspective. Aquatic Resources, Culture and Development, 12-pp.

[6] Péron, G., Mittaine, J. F., & Le Gallic, B. (2010). Where do fishmeal and fish oil products come from? An analysis of the conversion ratios in the global fishmeal industry. Marine policy, 34(4), 815-820.
[7] Korkut, A. Y., Kop, A., & Demir, P. (2007). Fish oil, used in fish feeds and its characteristics. Ege Journal of Fisheries and Aquatic Sciences, 24(1).
[8] Phung, A. S., Bannenberg, G., Vigor, C., Reversat, G., Oger, C., Roumain, M., ... & Wang, S. C. (2020). Chemical compositional changes in over-oxidized fish oils. Foods, 9(10), 1501.
[9] Boran, G., Karaçam, H., & Boran, M. (2006). Changes in the quality of fish oils due to storage temperature and time. Food chemistry, 98(4), 693-698.
[10] Hsieh, R. J., & Kinsella, J. E. (1989). Oxidation of polyunsaturated fatty acids: mechanisms, products, and inhibition with emphasis on fish. Advances in food and nutrition research, 33, 233-341.
[11] Wang, D., Xiao, H., Lyu, X., Chen, H., & Wei, F. (2023). Lipid oxidation in food science and nutritional health: A comprehensive review. Oil Crop Science.
[12] Vargas, F. C., Gómez, B., Mousavi Khaneghah, A., Strozzi, I., Gavahian, M., Barba, F. J., ... & Lorenzo, J. M. (2019). Assessment of the suitability of pitanga leaf extract as a natural antioxidant for enhancing canola oil stability: Monitoring lipid oxidation parameters. European Journal of Lipid Science and Technology, 121(5), 1800447.
[13] Sowbhagya, H. B. (2014). Chemistry, technology, and nutraceutical functions of celery (Apium graveolens L.): an overview. Critical reviews in food science and nutrition, 54(3), 389-398.
[14] Tint, S. S. Myint, S. H., & Than, N. N. (2021). Investıgatıon of Essentıal Oıl from the Leaf and Antıoxıdant Actıvıty of Plant Apıum graveolens l.(tayoke nan-nan). J. Myanmar Acad. Arts Sci, 19(1), 13-49.
[15] Hassanen, N. H., Eissa, A. M. F., Hafez, S. A. M., & Mosa, E. A. (2015). Antioxidant and antimicrobial activity of celery (Apium graveolens) and coriander (Coriandrum sativum) herb and seed essential oils. Int. J. Curr. Microbiol. App. Sci, 4(3), 284-296.
[16] Kesbiç, O. S., Parrino, V., Acar, Ü., Yilmaz, S., Paro, G. L., & Fazio, F. (2020). Effects of Monterey cypress (Hartw) leaf essential oil as a dietary supplement on growth performance and haematological and biochemical parameters of common carp (L.). Annals of Animal Science, 20(4), 1411-1426.
[17] Kesbiç, O. S. (2019). Effects of the cinnamon oil (Cinnamomum verum) on growth performance and blood parameters of rainbow trout (Oncorhynchus mykiss). Turkish Journal of Agriculture-Food Science and Technology, 7(2), 370-376.
[18] Sharma, O. P., & Bhat, T. K. (2009). DPPH antioxidant assay revisited. Food chemistry, 113(4), 1202-1205.
[19] Karami, H., Rasekh, M., & Mirzaee–Ghaleh, E. (2020). Comparison of chemometrics and AOCS official methods for predicting the shelf life of edible oil. Chemometrics and Intelligent Laboratory Systems, 206, 104165.
[20] Ellse, L., & Wall, R. (2014). The use of essential oils in veterinary ectoparasite control: a review. Medical and Veterinary Entomology, 28(3), 233-243.
[21] Manion, C. R., & Widder, R. M. (2017). Essentials of essential oils. American Journal of Health-System Pharmacy, 74(9), e153-e162.
[22] Fisher, K., & Phillips, C. (2008). Potential antimicrobial uses of essential oils in food: is citrus the answer?. Trends in food science and technology, 19(3), 156-164.
[23] Basmacioglu, H., Tokusoglu, Ö., & Ergül, M. (2004). The effect of oregano and rosemary essential oils or alpha-tocopheryl acetate on performance and lipid oxidation of meat enriched with n-3 PUFA's in broilers. South African Journal of Animal Science, 34(3).
[24] Frankel, E. N. (1984). Lipid oxidation: mechanisms, products and biological significance. Journal of the American Oil Chemists' Society, 61(12), 1908-1917.
[25] Schaich, K. M. (2020). Toxicity of lipid oxidation products consumed in the diet. Bailey's Industrial Oil and Fat Products; John Wiley and Sons: Hoboken, NJ, USA, 1-88.
[26] Jayasena, D. D., & Jo, C. (2014). Potential application of essential oils as natural antioxidants in meat and meat products: A review. Food reviews international, 30(1), 71-90.
[27] Franz, A. R., Knaak, N., & Fiuza, L. M. (2011). Toxic effects of essential plant oils in adult Sitophilus oryzae (Linnaeus)(Coleoptera, Curculionidae). Revista Brasileira de entomologia, 55, 116-120.
[28] Hrebień-Filisińska, A. M., & Bartkowiak, A. (2021). Antioxidative effect of sage (Salvia officinalis L.) macerate as "green extract" in inhibiting the oxidation of fish oil. Antioxidants, 11(1), 100.
[29] Kumari, A. J., Venkateshwarlu, G., Choukse, M. K., & Anandan, R. (2014). Effect of essential oil and aqueous extract of ginger (Zingiber officinale) on oxidative stability of fish oil-in-water emulsion. J Food Process Technol, 6(412), 2.
[30] Durmus, M., Özogul, Y., Ozyurt, G., Ucar, Y., Kosker, A. R., Yazgan, H., ... & Özogul, F. (2023). Effects of citrus essential oils on the oxidative stability of microencapsulated fish oil by spray-drying. Frontiers in Nutrition, 9, 978130.
[31] Gardner, H. W. (1983). Effects of lipid hydroperoxides on food components. Xenobiotics in foods and feeds, 63-84.

[32] Mozuraityte, R., Kristinova, V., Standal, I. B., Carvajal, A. K., & Aursand, M. (2016). Oxidative stability and shelf life of fish oil. In Oxidative stability and shelf life of foods containing oils and fats (pp. 209-231). AOCS Press.
[33] Rana, M., & Yadav, N. (2017). Celeriac, in Vegetable Crops Science: CRC Press, 939-952.
[34] Godlewska, K., Pacyga, P., Michalak, I., Biesiada, A., Szumny, A., Pachura, N., & Piszcz, U. (2020). Field-scale evaluation of botanical extracts effect on the yield, chemical composition and antioxidant activity of celeriac (Apium graveolens L. var. rapaceum). Molecules, 25(18), 4212.
[35] Fratta Pasini, A. M., & Cominacini, L. (2023). Potential Benefits of Antioxidant Phytochemicals on Endogenous Antioxidants Defences in Chronic Diseases. Antioxidants, 12(4), 890.
[36] Olmedo, R. H., Asensio, C., Nepote, V., Mestrallet, M. G., & Grosso, N. R. (2009). Chemical and sensory stability of fried-salted peanuts flavored with oregano essential oil and olive oil. Journal of the Science of Food and Agriculture, 89(12), 2128-2136.
[37] Emir Çoban, Ö., Patir, B., & Yilmaz, Ö. (2014). Protective effect of essential oils on the shelf life of smoked and vacuum packed rainbow trout (Oncorhynchus mykiss W. 1792) fillets. Journal of food science and technology, 51, 2741-2747.

doi:10.55385/kastamonujes.1298700 KUJES 9(1):17-32, 2023

Kastamonu University
Journal of Engineering and Sciences
e-ISSN 2667-8209
http://dergipark.gov.tr/kastamonujes

A Comparative Performance Analysis of Wireless Power Transfer with Parametric Simulation Approach

Mehmet Cicek[a], Selami Balci[b*], Kadir Sabanci[b]

[a] Department of Electrical and Electronics Engineering, Institute of Science, Gazi University, Ankara, Türkiye
[b] Department of Electrical and Electronics Engineering, Faculty of Engineering, Karamanoglu Mehmetbey University, Karaman, Türkiye
***Corresponding Author:** sbalci@kmu.edu.tr

Received: **May 17, 2023** ◆ Accepted: **June 19, 2023** ◆ Published Online: **June 21, 2023**

Abstract: This paper presents using a parametric technique optimise and normalise approach for coreless Resonant Inductive Coupling Wireless Power Transfer (RIC-WPT) systems. The system under consideration is based on a compensated series-series (SS) circuit employing flat spiral coils. Moreover, the proposed approach aims to determine the optimal values for capacitors to achieve maximum efficiency during the operation of the RIC-WPT system. Three-dimensional (3D) flat spiral coils are modelled and subjected to parametric analysis with varying air-gaps using ANSYS-Electronics-Maxwell software with the Finite Element Method (FEM). Subsequently, a power electronics circuit employing a full-bridge inverter is designed using ANSYS-Simplorer software. The coils and the power electronics circuit are co-simulated with different parameter values. Consequently, based on the findings of the parametric simulation studies, the most efficient configuration for a Wireless Power Transfer (WPT) system is proposed, incorporating the design and standardization of power electronics components suitable for the specified operating frequency. The simulation results indicate that power transmission with an efficiency of approximately 74.31% is achieved when the air gap between the coils is set to 200 mm. Moreover, the co-simulation studies, involving different parametric values in power electronics circuit parameters and electromagnetic modelling parameters, provide valuable insights for WPT designs.

Keywords: Co-simulation, FEM, parametric simulation, wireless power transfer.

Öz: Bu makale, nüvesiz Rezonant Endüktif Kuplaj Kablosuz Güç Aktarımı (RIC-WPT) sistemlerini optimize etmek ve standart hale getirmek için parametrik tekniklerin kullanımını sunmaktadır. Ele alınan sistem, düz spiral bobinler kullanan kompanze edilmiş bir seri-seri (SS) devreye dayanmaktadır. Ayrıca, önerilen yaklaşım, RIC-WPT sisteminde maksimum verim elde etmek için kapasitörler için en uygun değerleri belirlemeyi amaçlamaktadır. Üç boyutlu (3D) yassı spiral bobinler, Sonlu Elemanlar Metodu (SEM) ile ANSYS-Electronics-Maxwell yazılımı kullanılarak modellenmiş ve farklı hava aralıklarıyla parametrik analize tabi tutulmuştur. Daha sonra, ANSYS-Simplorer yazılımı kullanılarak tam köprü evirici kullanan bir güç elektroniği devresi tasarlanmıştır. Bobinler ve güç elektroniği devreleri, farklı parametre değerleri ile simüle edilmiştir. Sonuç olarak, parametrik simülasyon çalışmalarının bulgularına dayanarak, belirtilen çalışma frekansına uygun güç elektroniği bileşenlerinin tasarımını ve standardizasyonunu içeren bir Kablosuz Güç Aktarımı (WPT) sistemi için en verimli konfigürasyon önerilmiştir. Simülasyon sonuçları, bobinler arası boşluk 200 mm olarak ayarlandığında yaklaşık %74,31 verimle güç iletiminin elde edildiğini göstermektedir. Ayrıca, güç elektroniği devre parametrelerinde ve elektromanyetik modelleme parametrelerinde farklı parametrik değerleri içeren eşanlı benzetim çalışmaları, WPT tasarımları için değerli bilgiler sunmaktadır.

Anahtar Kelimeler: Eş-benzetim, SEM, parametrik benzetim, kablosuz güç aktarımı.

1. Introduction

Wireless power transfer (WPT) systems have gained considerable attention in various domains, ranging from everyday devices such as toothbrushes to advanced applications like spacecraft. Resonant inductive coupling wireless power transfer (RIC-WPT) [1] represents a wireless power transfer technique that enables the transmission of electrical energy through an electromagnetic field, eliminating the need for physical connections [2–4]. This concept was initially proposed and patented by Nikola Tesla in the early 20th century [3, 5–7], sparking scientific interest and research in WPT systems over the past century.

Masers and the maser communication system marked the initial milestones in the development of far-field Wireless Power Transfer (WPT) systems in 1960 [8]. Within a decade, lasers emerged as a viable solution for far-field WPT applications [9]. Moreover, in 1969, William C. Brown invented a microwave WPT system [10]. Despite the height constraint of 15.44 m, Brown successfully transferred 270 W of power via microwave to a prototype aircraft [11]. Kimura et al. proposed a miniature opto-electric transformer for optical WPT approaches [12]. Sahai and Graham suggested a device incorporating a laser-diode array for optical WPT systems [13]. Ishiyama et al. explored the use of an ultrasonic air transducer for WPT

[14]. Approximately a century after Tesla's initial presentation, Kurs et al. introduced and conducted experiments with a novel Resonant Inductive Coupling Wireless Power Transfer (RIC-WPT) system. Led by Professor M. Soljačić, this research team achieved the transfer of 60 W of power with an efficiency of 40% over a distance exceeding 2 m between the transmitter and receiver [15]. Following this significant advancement, the interest in WPT has been further amplified.

Canon et al. used only one transmitter coil for multiple loads [16]. Karakaya transferred power to the DC motor with 60% efficiency by WPT. He also sent the motor rotation direction information of the DC motor within this power [17].

Canon et al. employed a single transmitter coil to power multiple loads in their study [16]. Karakaya successfully achieved power transfer to a DC motor with an efficiency of 60% using WPT. Additionally, he transmitted information about the rotational direction of the DC motor alongside the power transfer [17].

Over time, researchers have proposed various strategies to enhance the efficiency of WPT systems. These approaches encompass the utilization of auxiliary coils [4, 18–20], the development of novel mathematical models [21–25], the design of advanced control circuits [1, 26–29], the application of machine learning techniques [30–35], and the modification of geometric structures [36–43]. These endeavours have aimed to optimize the performance and effectiveness of WPT systems in an academic and formal context.

In the past two decades, there has been a remarkable surge in the popularity of electric vehicles, consequently creating a new realm for Wireless Power Transfer (WPT) systems. This development has attracted the attention of numerous researchers and prominent technology companies, leading to extensive exploration and advancements in this emerging field [44–49].

This paper introduces a parametric optimization and normalization methodology for coreless Resonant Inductive Coupling Wireless Power Transfer (RIC-WPT) systems. The proposed system is built upon a series-series (SS) compensated circuit utilizing flat spiral coils, operating at a frequency of 86 kHz. The selection of this specific operating frequency aligns with the standard set forth by the Society of Automotive Engineers (SAE) in their SAE J2954 guidelines.

2. Classifying of Wireless Power Transfer

In wireless power transfer (WPT) systems, the notion of a "media" or "carrier field" arises, representing the energy form through which power is converted and transmitted. Based on the investigations conducted, WPT systems can be categorized into distinct research domains, as depicted in Figure 1, depending on the type of carrier field employed [47], [50, 51].

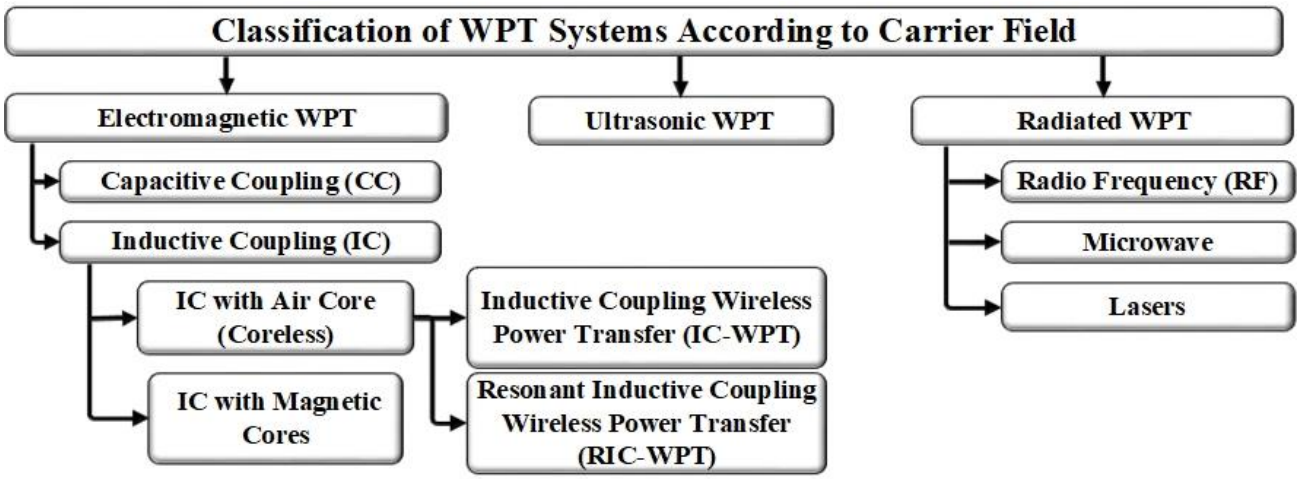

Figure 1. Classification of WPT systems according to carrier field [52].

Additionally, the power transfer distance serves as a crucial parameter for classifying Wireless Power Transfer (WPT) systems. Therefore, WPT systems can be categorized into distinct research areas, as illustrated in Figure 2 [47, 53, 54].

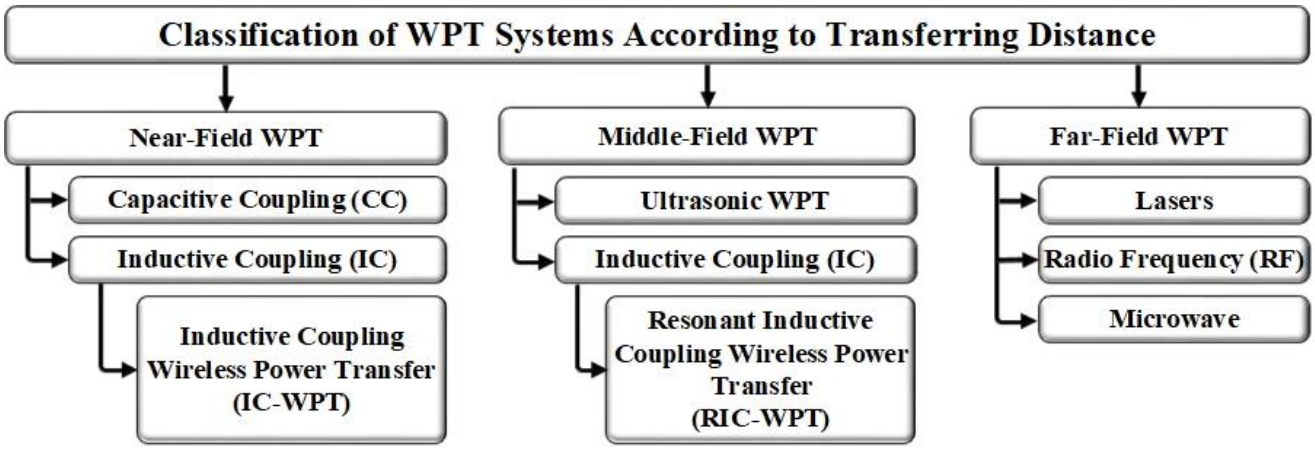

Figure 2. Classification of WPT systems according to transferring distance [52].

Simultaneously, Wireless Power Transfer (WPT) systems can be classified based on the number of loads and sources they involve. Circuits with a single source and a single load are referred to as Single Input - Single Output (SISO). Similarly, circuits with a single source and multiple loads are categorized as Single Input - Multiple Output (SIMO). On the other hand, circuits with multiple sources and a single load are termed as Multiple Input - Single Output (MISO), and circuits with multiple sources and multiple loads fall under the classification of Multiple Input - Multiple Output (MIMO) [55]. Figure 3 illustrates these circuit models, where "T_x" represents the transmitter circuit, "R_x" represents the receiver circuit, "R_s (Ω)" denotes the source resistance, "C_t (F)" signifies the resonant capacitor of the transmitter, "L_t (H)" represents the transmitter coil, "Rt (Ω)" signifies the inner resistance of the transmitter coil, "L_t (H)" represents the receiver coil, "R_r (Ω)" signifies the inner resistance of the receiver coil, "C_r (F)" denotes the resonant capacitor of the receiver circuit, "R_L (Ω)" represents the load, and "M (H)" stands for mutual inductance.

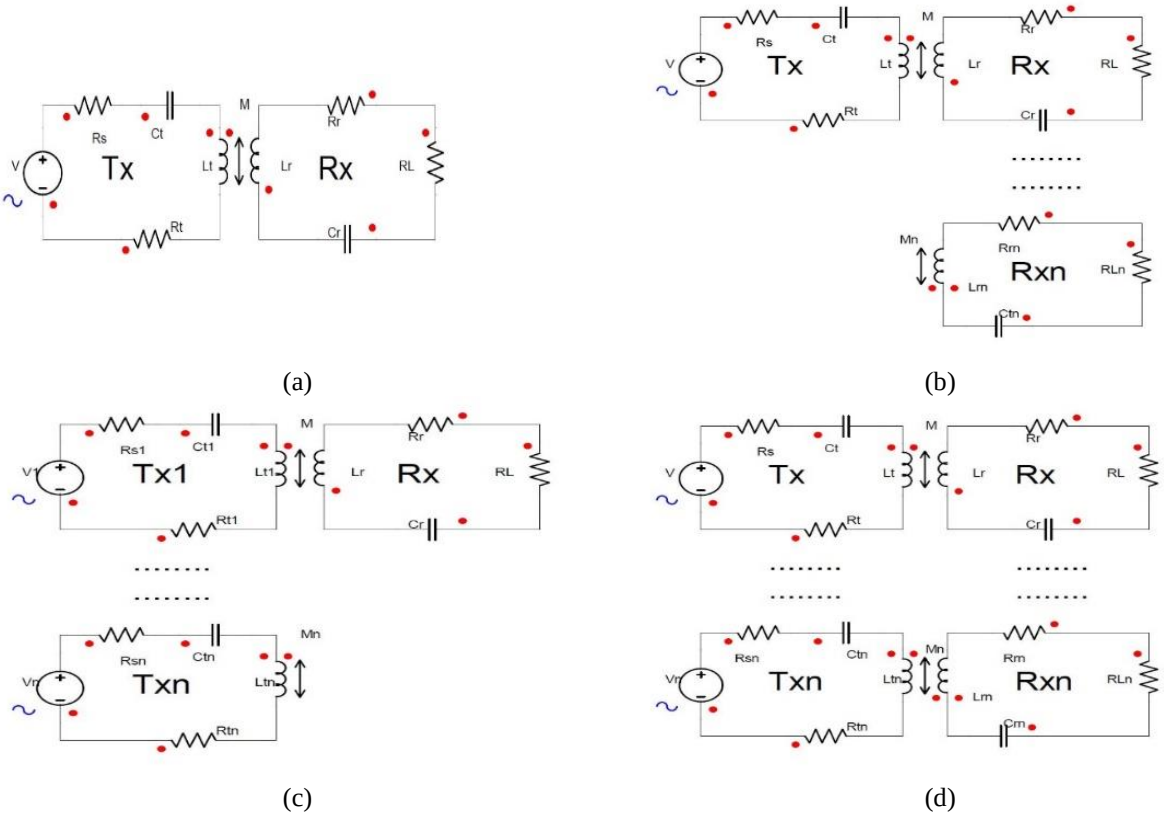

Figure 3. Circuit models of WPT systems, **(a)** SISO circuit model, **(b)** SIMO circuit model, **(c)** MISO circuit model, **(d)** MIMO circuit model.

The final parameter for categorizing WPT systems is the compensation type employed in the transmitter and receiver circuits. There exist four fundamental types of compensation: Serial Transmitter - Serial Receiver (SS), Serial Transmitter - Parallel Receiver (SP), Parallel Transmitter - Serial Receiver (PS), and Parallel Transmitter - Parallel Receiver (PP) compensated circuit models [21, 47]. Figure 4 illustrates these circuit models.

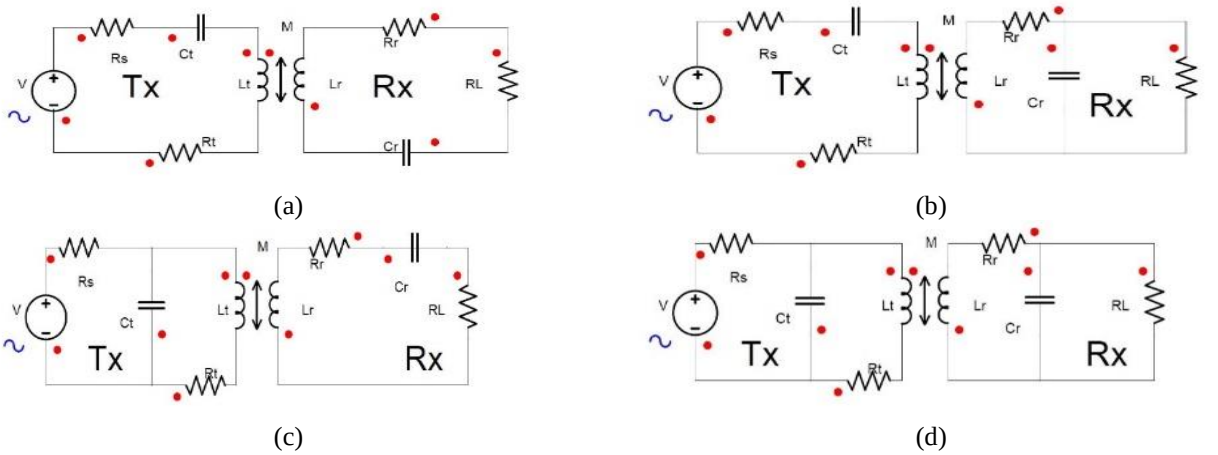

Figure 4. Circuit models of WPT systems, **(a)** SS compensated circuit, **(b)** SP compensated circuit, **(c)** PS compensated circuit, **(d)** PP compensated circuit.

3. Modelling of the WPT Circuit

The modelling of wireless power transfer involves an initial examination of the fundamental circuit equations. Subsequently, comprehensive calculations, design, and analysis of the employed WPT system have been conducted.

The Basic Equations for WPT

The concept behind the RIC-WPT system revolves around the utilization of capacitors and coils during the resonance period. During this phase, the capacitive reactance (X_C) is equated to the inductive reactance (X_L). The angular frequency (ω_0) at the point of resonance can be determined using Equation 1:

$$X_L = X_C \Rightarrow \omega_0 L = \frac{1}{\omega_0 C} \Rightarrow \boxed{\omega_0 = \frac{1}{\sqrt{LC}}} \quad (1)$$

The resonant frequency (f_0) is given in Eq. 2:

$$\omega_0 = 2\pi f_0 = \frac{1}{\sqrt{LC}} \Rightarrow \boxed{f_0 = \frac{1}{2\pi\sqrt{LC}}} \quad (2)$$

Also, Figure 5 illustrates two magnetically interconnected coils and the overall system they comprise [4], [56]. The transfer of power occurs from inductor L_1 to inductor L_2 through magnetic coupling.

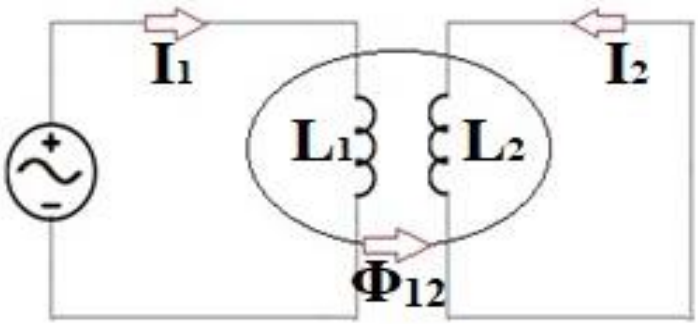

Figure 5. Two coils magnetically connected by common flux Φ_{12} [4, 56]

The magnetic flux, denoted as Φ_{12} (Wb), originates from the current I_1 (A). However, the presence of the L_2 coil has a significant impact on the overall system. As a result, the magnetic flux Φ_{12} (Wb) undergoes a constant change, as described in Eq. 3. This constant is referred to as "Mutual Inductance," with its SI unit being Henry (H), symbolized by M, as indicated in Eq.3 [57].

$$\Phi_{12} = M.I_1 \tag{3}$$

Through extensive research on Wireless Power Transfer (WPT), practical methodologies have been developed to calculate the mutual inductance based on the specific geometric configurations employed. Equation 4 represents the mathematical expression utilized for determining the mutual inductance in the context of two single-winding wire coils. In this equation, denoted as Eq.4 [46, 52, 58–62], M0 (μH) represents the mutual inductance, while a (m) and b (m) correspond to the radii of the transmitter and receiver coils, respectively. Furthermore, K(c) and E(c) denote the complete elliptic integrals of the first and second order, respectively, with respect to the parameter c.

$$M_0 = \mu_0 \frac{\sqrt{ab}}{\sqrt{c}}\left[(2-c)K(c) - 2E(c)\right] \tag{4}$$

Where d (m) is the distance between transmitter and receiver coils as given in Eq.5:

$$c = \frac{4ab}{(a+b)^2 + d^2} \qquad K(\varphi, c) = \int_0^{\varphi} \frac{d\varphi}{\sqrt{1-c^2.\sin^2\varphi}} \qquad E(\varphi, c) = \int_0^{\varphi} \sqrt{1-c^2.\sin^2\varphi}.d\varphi \tag{5}$$

Thus, Eq.4 provides the mutual inductance between two single-turn loops. However, for coils with multiple turns, denoted by N_1 and N_2 representing the number of turns, the mutual inductance M is given by Eq.6.

$$M = M_0 N_1 N_2 \tag{6}$$

In WPT systems, there is another constant which is expresses the effectiveness of the magnetic coupling between the coils to indicate how much of the transmitted power, that is, the flux, reaches the receiver. This constant is called the coupling coefficient. This constant is denoted by the letter “k” [56]. K takes values between 0 and 1 and is defined as given in Eq.7: In Wireless Power Transfer (WPT) systems, the efficacy of the magnetic coupling between the coils, which determines the proportion of transmitted power (flux) received by the receiver, is quantified by a parameter known as the coupling coefficient. The coupling coefficient is denoted by the symbol "k" [56]. It assumes values between 0 and 1 and is mathematically defined as shown in Eq.7.

$$k = \frac{M}{\sqrt{L_t L_r}} \tag{7}$$

Calculation of the WPT Coils

Previous literature has documented various coil shapes, such as the conventional rectangular coil, rectangular double loop coil, hexagonal coil, and cloverleaf, in the context of wireless power transfer (WPT) systems. The geometric configuration of the coils employed in WPT circuits significantly impacts their performance [63]. In this study, flat spiral coils are utilized as both transmitter and receiver coils, as depicted in Figure 6.

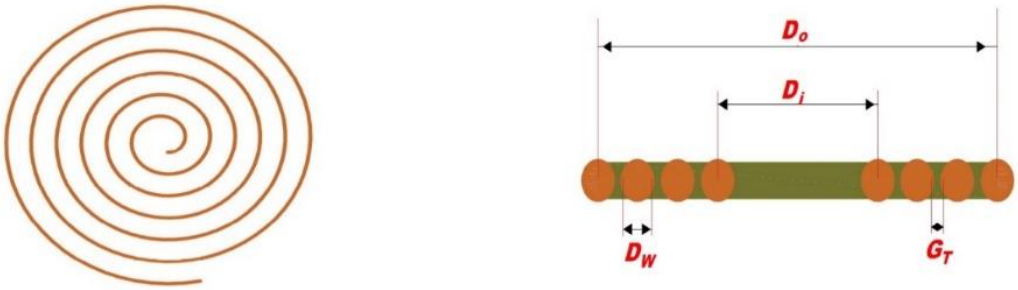

(a) **(b)**

Figure 6. The geometric structure of the WPT coils, **(a)** Flat spiral coil, **(b)** Flat spiral coil variables [52].

The inductance of the coil, L (μH), is defined [4, 52, 64–66] as seen in Eq.8:

$$A=\frac{D_i+N\left(D_W+G_T\right)-G_T}{2};L=\frac{N^2.A^2}{30.A-11.D_i}(\mu H) \quad (8)$$

The inside diameter of the coil, denoted as Di (m), along with the wire diameter represented by DW (m), and the distance between wire turns, indicated as GT (m), are crucial parameters. Additionally, the number of turns is denoted by N. The length of the wire used in the coil, l_w (m), can be calculated using Eq. 9 [66].

$$l_W=\beta\frac{\pi}{2}N(D_i+D_o) \quad (9)$$

β is the twist factor coefficient which is 1.02 [65]. D_O (m) is the outer diameter of the coil and defined [66] by Eq.10:

$$D_O=\left[D_i+2N\left(D_W+G_T\right)-2G_T\right] \quad (10)$$

The DC resistance, R_{DC} (Ω), of a wire, where (S/m) is the electrical conductivity, and A_W (m2) is the area of the wire cross-sectional area, is calculated [57, 67] by Eq.11:

$$R_{DC}=\frac{l_W}{\sigma.A_W} \quad (11)$$

The frequency could be easily added to calculations with the use of electrical conductivity. Because the skin depth, δ (m), and the electrical conductivity, (S/m), are related to each other [57] by Eq.12:

$$\delta=\frac{1}{\sqrt{\pi f\mu\sigma}} \quad (12)$$

Where μ (H/m), is the magnetic permeability, and *f* (Hz) is the frequency. Thus the total resistance of the coil, R_W (Ω), is calculated by Eq.13:

$$R_W=\frac{l_W}{\sigma A_W}\left(\frac{1}{4}+\frac{r_W}{2\delta}\right) \quad (13)$$

Design of the Circuit

In this research, the resonant inductive coupling wireless power transmission (RIC-WPT) method is employed, utilizing the series-series (SS) compensated and single-input single-output (SISO) circuit model depicted in Figure 4(a). The circuit analysis is conducted using the equivalent circuit model illustrated in Figure 7. The variable I_s (A) represents the current in the transmitter circuit, while I_L (A) denotes the current in the receiver circuit.

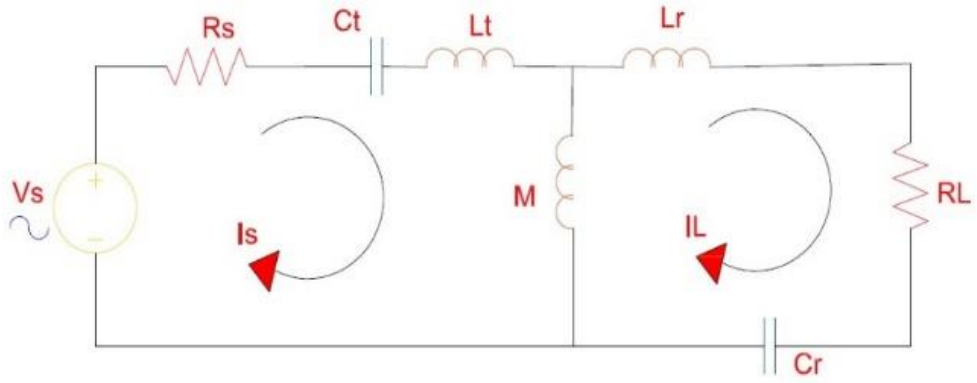

Figure 7. Equivalent circuit model of the WPT system [21–23, 41].

According to Kirchhoff' voltage law, we can express, as stated in Eq.14 [52] for Figure 7:

$$\begin{pmatrix} V_S \\ 0 \end{pmatrix} = \begin{pmatrix} R_S + j\left(\omega L_t - \dfrac{1}{\omega C_t}\right) & -j\omega M \\ -j\omega M & R_L + j\left(\omega L_r - \dfrac{1}{\omega C_r}\right) \end{pmatrix} \cdot \begin{pmatrix} I_S \\ I_L \end{pmatrix} \quad (14)$$

At the resonant moment ($X_C = X_L$) with Eqs.15-16, and the efficiency (η) of the WPT system in Eq.17:

$$I_S = \frac{V_S.\left(R_L + R_r\right)}{R_t.\left(R_L + R_r\right) + \omega^2 M^2} \quad (15)$$

$$I_L = -\frac{j\omega M V_S}{R_t.\left(R_L + R_r\right) + \omega^2 M^2} \quad (16)$$

$$\eta = \left(\frac{I_L}{I_S}\right)^2 . \frac{\left(R_L + R_r\right)}{Z_I} = \frac{\omega^2 M^2}{R_t.\left(R_L + R_r\right) + \omega^2 M^2} \quad (17)$$

4. Simulation Studies

Before conducting the simulation studies, initial values were determined and listed in Table 1. Subsequently, a Matlab code is developed with parametric values based on the number of turns of the coils, aiming to design the most efficient coil system.

Table 1. Known initial values of the design.

Description	Symbol	Value
The operating frequency	f	86 kHz
The diameter of the wire	D_w	16 mm
The voltage of the source	V_s	12 V
Load	R_L	5 Ω
The distance between the coil turns	G_t	3 mm
The inside diameter of the coil	D_i	10 mm

The number of turns of the transmitter coil is denoted as N_t, while the number of turns of the receiver coil is denoted as N_r, as indicated in Table 2.

Table 2. Parametric values of the WPT coils.

Parameters	N_t	N_r
Parametric Range	5-10	5-20
Linear Step	5	5

After the calculations, it is determined that the most efficient winding number was obtained when $N_r = 20$ and $N_t = 10$. I_s (A) is the transmitter circuit current, I_L (A) is the receiver circuit current, V_L (V) is the voltage value on the load, P_i(W) is the input power, P_O(W) is the output power, and η (%) is the efficiency in Table 3.

Table 3. The most efficient number of the turns of the coils.

N_t	N_r	L_t (uH)	L_r (uH)	I_S (A)	I_L (A)	V_L (V)	P_i(W)	P_0(W)	η (%)
10	20	13.4263	103.5367	70.6	12.59	62.96	847	793	93.61

The coil system design is created in 3D using the calculated values within the model specified in the ANSYS-Electronics-Maxwell software. Figure 8 illustrates the complete coil system, with the receiver coil represented by the larger coil and the transmitter coil represented by the smaller coil.

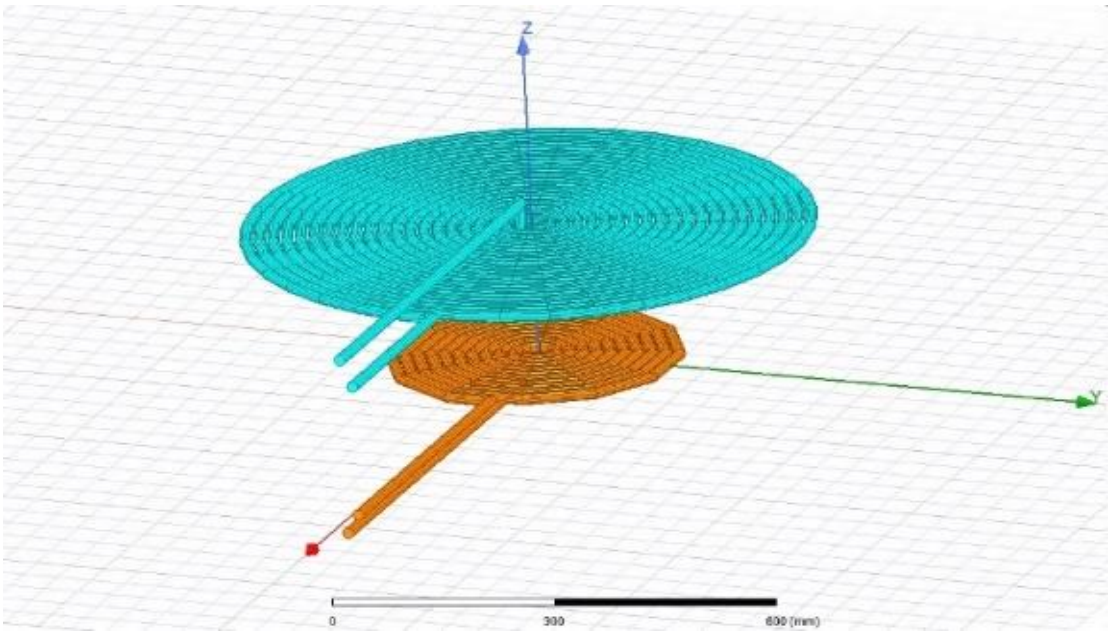

Figure 8. Maxwell 3D coil system

The spacing between the coils, denoted as 'z_space' (mm), is systematically varied from 50 mm to 500 mm with a linear increment of 50 mm. In wireless power transfer (WPT) systems, there exists a linear relationship between efficiency and the coupling coefficient. Hence, the impact of the spacing, as depicted in Figures 9 and 10, on the coupling coefficient and mutual inductance is investigated.

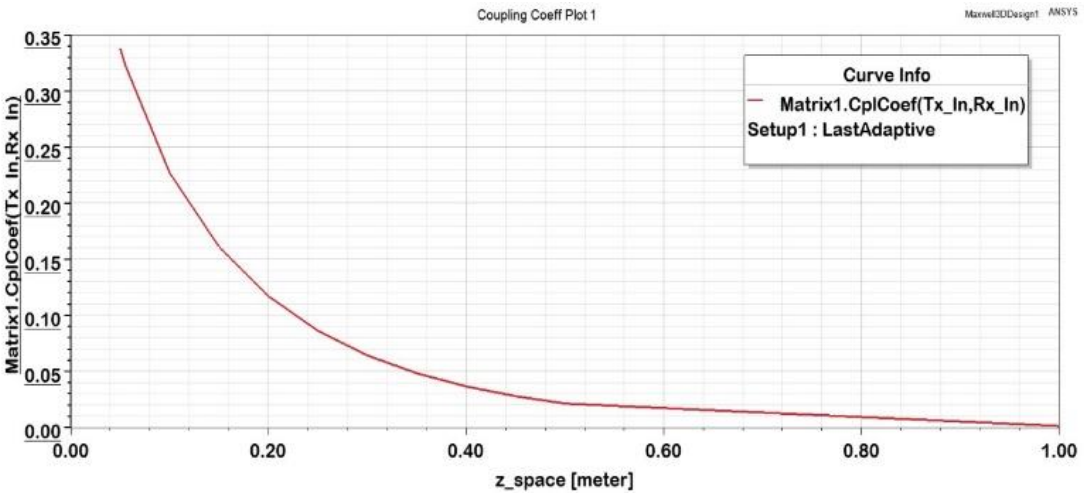

Figure 9. The parametric effect of the distance on the coupling coefficient.

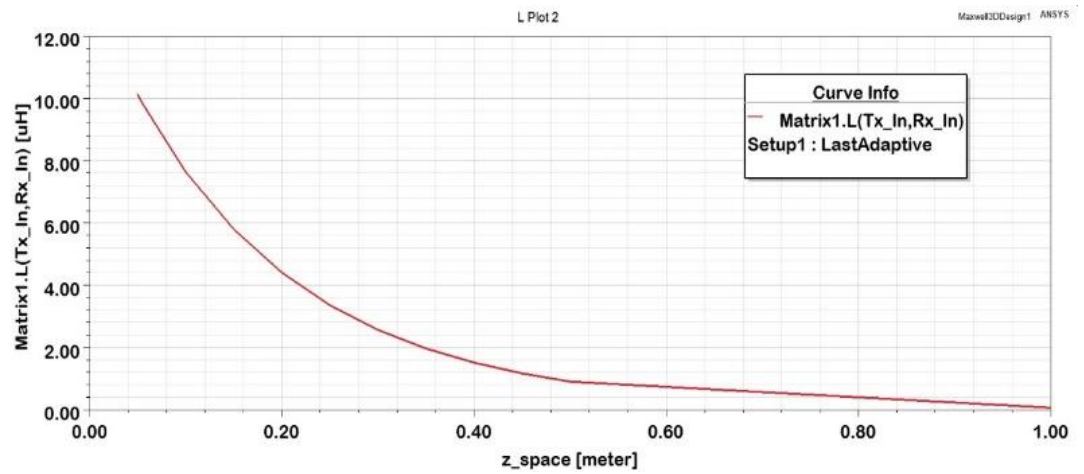

Figure 10. The parametric effect of the distance on the mutual inductance.

Table 4 illustrates the variation of values about distance, showcasing the dynamic nature of the designed coil system. Subsequently, the coil system is integrated into the power electronics circuit, which is developed using ANSYS-Simplorer software, allowing for co-simulation with ANSYS-Maxwell. The comprehensive WPT system is depicted in Figure 11.

Table 4. Effect of the distance on mutual inductance and coupling coefficient

z_space (mm)	**50**	**100**	**150**	**200**	**250**	**300**	**350**	**400**	**450**	**500**	**1000**
M(uH)	10.12	7.64	5.80	4.41	3.36	2.57	1.97	1.52	1.18	0.917	0.081
k	0.337	0.227	0.161	0.117	0.086	0.064	0.048	0.037	0.028	0.021	0.0018

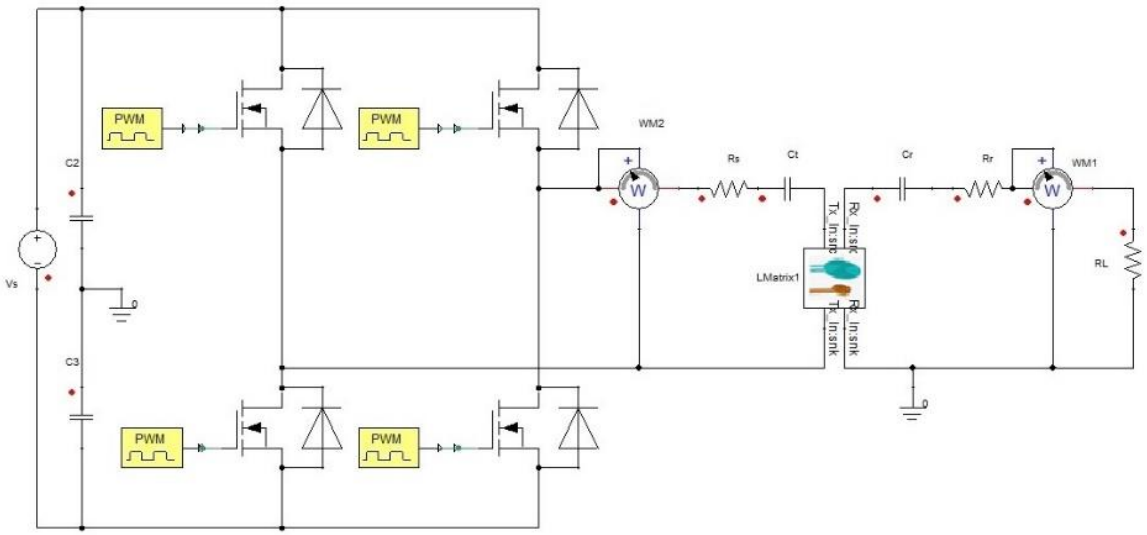

Figure 11. Power electronics circuit of the entire WPT system [41].

Initially, the circuit is co-simulated using calculated values in MATLAB. Both the input power and output power are observed during the simulation. Figure 12 depicts the input power [Pi (W)], while Figure 13 illustrates the output power [Po (W)].

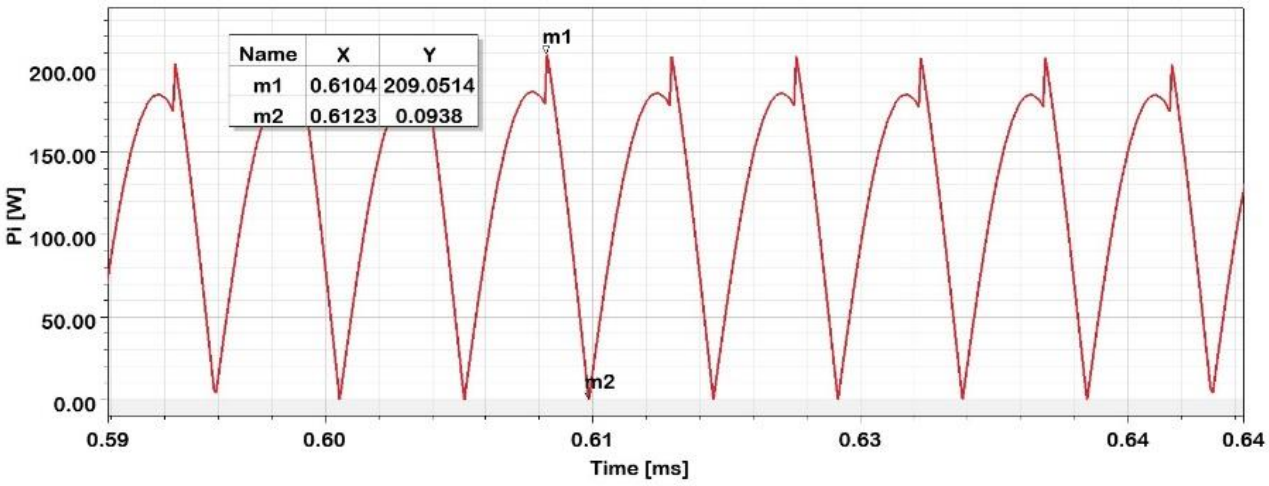

Figure 12. P_i (W) with calculated values co-simulation result.

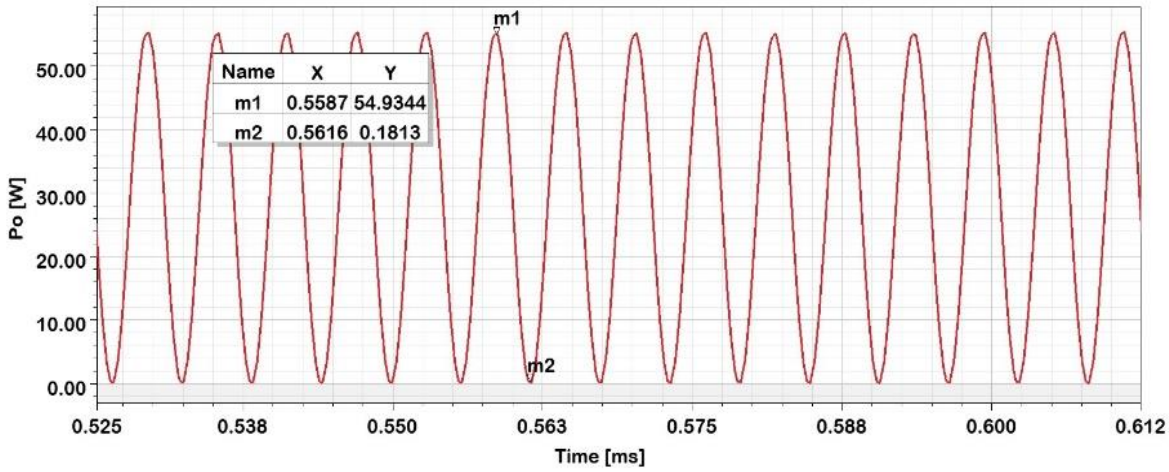

Figure 13. P_o (W) with calculated values co-simulation result.

Table 5 displays the observed values and corresponding efficiency in this case. Additionally, for the parametric studies, four variables have been chosen: capacitors (C_t, C_r), the distance between coils (z_space), operating frequency (f), and load (R_L). All these variables, along with their respective parameter values, are presented in Table 6.

Table 5. The results observed in the study which is made with the calculated values.

Variables	Values	Units
C_t	255.086	nF
C_r	33.078	nF
P_i	200	W_p
P_o	55	W_p
η (%)	27.5	

Table 6. WPT parametric values.

Variable Names	Calculated Values	Units	Parametric Range	Linear Step
z_space	200	mm	50 - 500	50
f	86	kHz	70 - 100	1
R_L	5	**Ω**	1 -20	1
C_t	255	nF	175 - 325	5
C_r	33	nF	20 - 150	5

Therefore, a total of 5,189,400 distinct possibilities are intended to be explored in this study. However, due to the limitation of ANSYS-Simplorer software, which can handle a maximum of 32,000 possibilities, the study has to be divided into four parts. The initial part focuses on the normalization of capacitor values. Figure 14 illustrates the relationship between efficiency and variations in capacitor values.

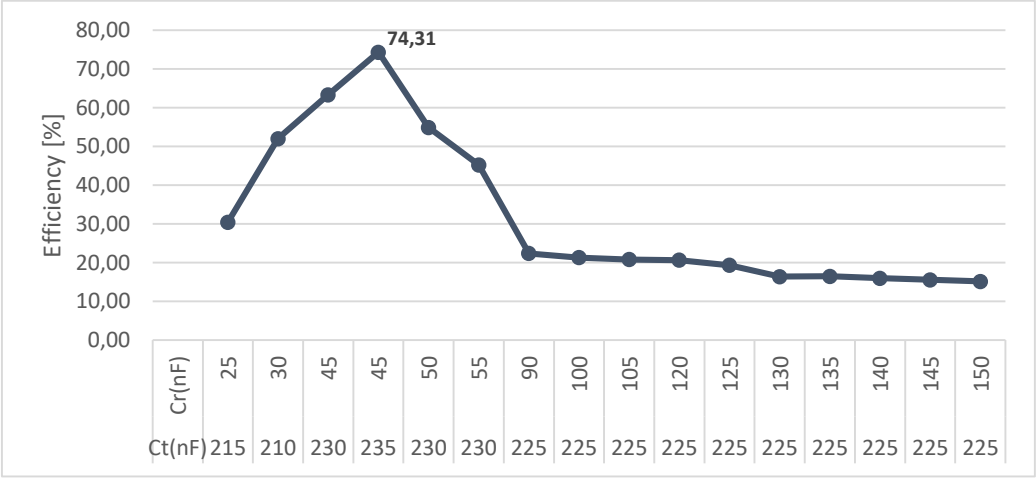

Figure 14. Efficiency characteristic vs. the parametric capacitor values.

The subsequent stage involves determining the optimal distance between coils (z_space) for achieving maximum efficiency. The capacitor values obtained from the previous phase are utilized in this analysis. The relationship between efficiency and distance variation is illustrated in Figure 15.

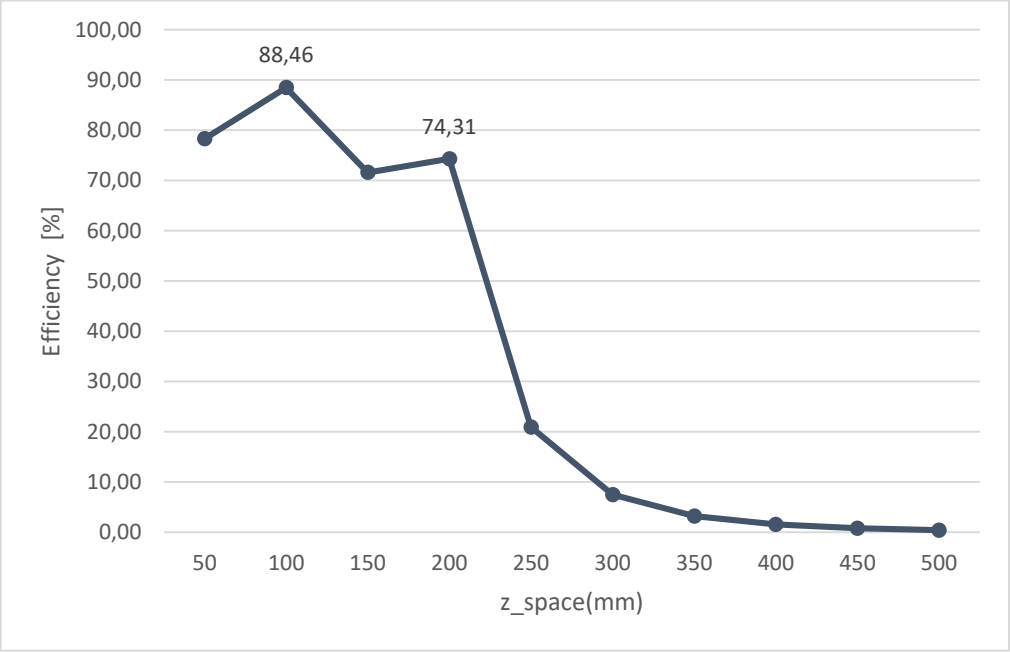

Figure 15. Efficiency characteristic vs. the parametric z_space (mm) values.

The optimal distance, as indicated in Table 7, for achieving the highest efficiency is 100 mm. Nevertheless, it should be noted that the output power reaches its maximum value when the distance between the coils is set to 200 mm.

Table 7. Efficient and power values for different z_space values

z_space (mm)	P_i (W_{rms})	P_0 (W_{rms})	η (%)
100	72.56	64.19	88.46
200	519.29	385.89	74.31

The third phase of the study involves altering the load value while keeping the chosen capacitor values and the optimal z_space value constant. This enables the easy observation of the efficiency variation in response to changes in the load. Figure 16 illustrates the relationship between efficiency and load variations, allowing for straightforward analysis.

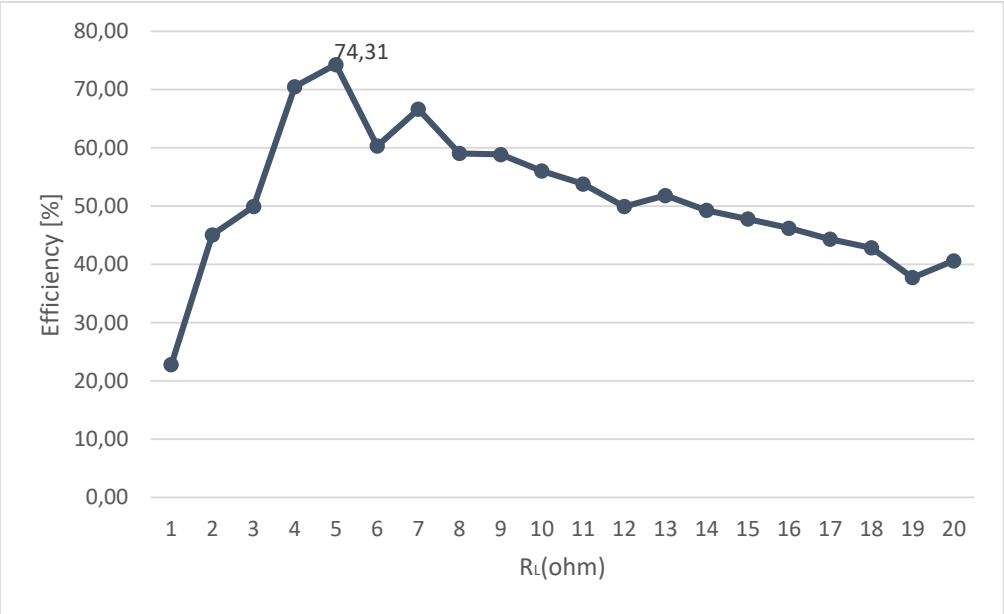

Figure 16. Efficiency characteristic vs. the parametric z_space (mm) values.

The fourth phase of the study involves the determination of the operating frequency, with all other parameters having been established. The operating frequency has been analyzed based on both calculated values and empirical observations. Figure 17 illustrates the relationship between the output power and various frequency values using the calculated capacitor values.

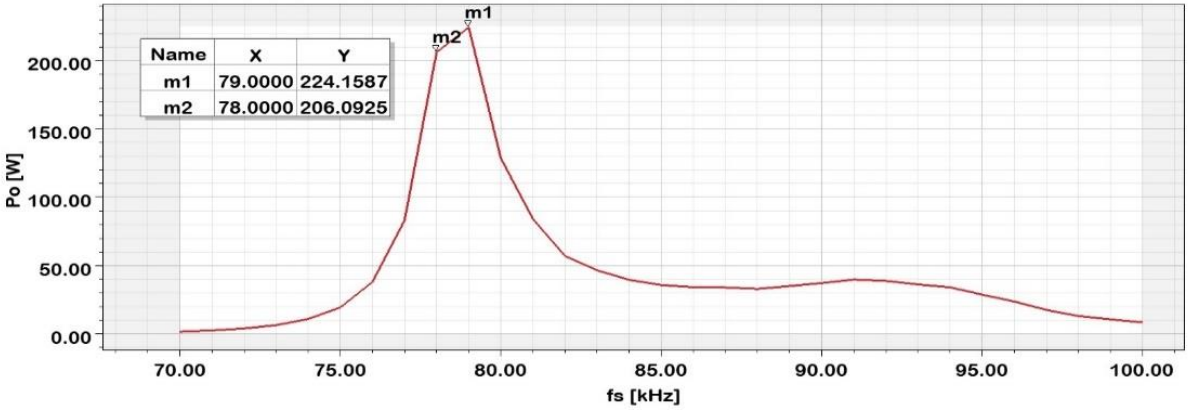

Figure 17. Po (W) vs. the parametric frequency values with calculated capacitor values.

Likewise, Figure 18 shows the output power with the determined capacitor values against different frequency values.

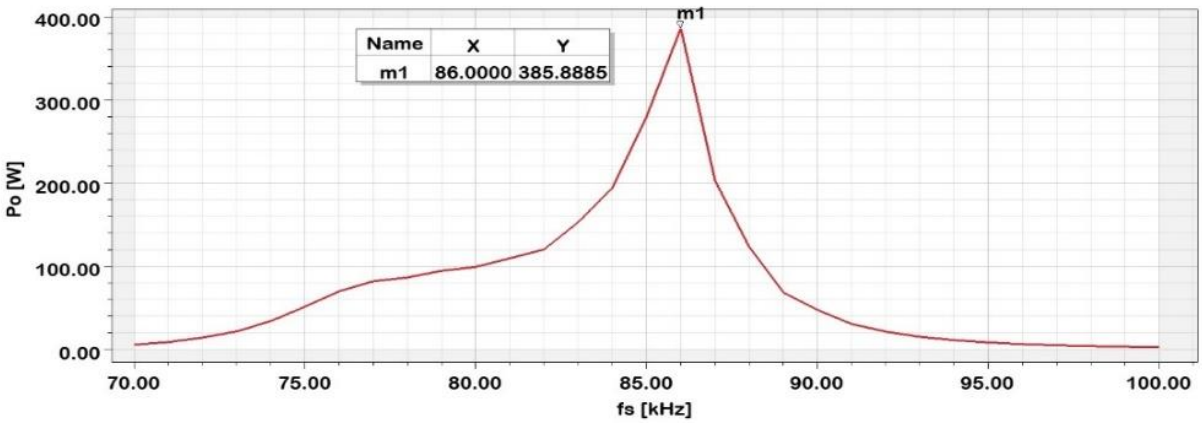

Figure 18. Po (W) vs. the parametric frequency values with calculated capacitor values.

Lastly, a final simulation was conducted to assess the benefits of the parametric approach. A new power electronics circuit was designed in ANSYS-Simplorer, omitting the co-simulation aspect. Subsequently, the circuit was simulated using Simplorer' built-in components. The efficiency results of the three studies are presented in Table 8.

Table 8. The comparison of the results.

Studies	**P_i (W_{rms})**	**P_0(W_{rms})**	**η (%)**
Calculation result	847	793	93.61
Results without co-simulation	848.52	594	70.39
Results with Parametrically co-simulation	519.29	385.88	74.31

The efficiency for WPT is highly affected by parameters such as the distance between transmit and receive coils, the coupling coefficient and resonance. Compared with the estimation studies based on simulations with parameters such as distance between the coils, alignment errors, in the studies conducted for the estimation of the efficiency [32, 41, 47]. Also, the efficiency value obtained in this study, with a rate of approximately 75%, suggests the parametric simulation approach as a very useful method for designers. Essentially, the efficiency does not depend only on the design of the coils and the distances between them. The efficiency of the power electronics circuit is very effective in this regard and should be considered together with the coil design.

5. Conclusion

This study introduces and analyses a wireless power transfer model through the process of definition, design, and parametric analysis. The system design calculations are performed using Matlab software in a parametric manner. It is observed that the results obtained from the equations used for calculations related to the flat spiral coil, mutual inductance, and coupling coefficient align closely with the simulation results. As a result, it is concluded that these equations can be effectively employed in future research on wireless power transfer.

The proposed method for WPT design demonstrates superior efficiency compared to the components available in ANSYS-Simplorer software and offers the advantage of simplified implementation with standardized components. Moreover, contrary to the conventional assumption that increasing the current on the transmitter side would lead to increased power on the receiver side, different outcomes have been obtained. It is determined that the power electronics circuit elements, correctly identified through parametric analysis, draw less current from the power source.

As a foundation for future studies in the field, it has been established that the design and operation of the coil should be conducted through co-simulation, while the determination of power electronics components should be based on parametric analysis using the computed outcomes. It is worth noting that, to achieve a constant load, all circuit parameters should be adjusted or normalized concerning a specific value.

Competing Interest / Conflict of Interest

The authors declare that they have no competing interests.

Author Contribution

We declare that all Authors equally contribute.

6. References

[1] Konishi, A., Umetani, K., & Hiraki, E. (2018, May). High-frequency self-driven synchronous rectifier controller for WPT systems. In 2018 International Power Electronics Conference (IPEC-Niigata 2018-ECCE Asia) (pp. 1602-1609). IEEE.

[2] Siddiqui, A., Nagani, A., & Ali, R. (2015). Wireless power transfer techniques: a review. Recent & Innovation Trends in Computing & Communication, 3(12), 6711-616.

[3] Tesla, N. (1905). Art of Transmitting Electrical Energy through the Natural Medium.

[4] Nisshagen, M., & Sjöstrand, E. (2017). Wireless power transfer using resonant inductive coupling-Design and implementation of an IPT system with one meter air gap in the region between near-range and mid-range..

[5] Tesla, N. (1900). System of Transmission of Electrical Energy, pp. 1–6, [Online]. Available: https://patentimages.storage.googleapis.com/62/90/92/45a5932052a940/US645576.pdf

[6] Tesla, N. (1900). Apparatus for Transmission of Electrical Energy.

[7] Tesla, N. (1898). "High Frequency Oscillators for Electro-Therapeutic and Other Purposes," Proc. IEEE, 87(7), 1282.

[8] Schawlow, A. L., & Townes, C. H. (1960). U.S. Patent No. 2,929,922. Washington, DC: U.S. Patent & Trademark Office.

[9] Maiman, T. H. (1967). Ruby laser system, pp. 3, 353, 115.
[10] Brown, W.C., (1969). Microwave to DC Converter.
[11] Brown, W.C. (1965). Experimental Airborne Microwave Supported Platform.
[12] Kimura, M., Miyakoshi, N., & Daibou, M. (1991, January). A miniature opto-electric transformer. In [1991] Proceedings. IEEE Micro Electro Mechanical Systems (pp. 227-232). IEEE.
[13] Sahai, A., & Graham, D. (2011, May). Optical wireless power transmission at long wavelengths. In 2011 International Conference on Space Optical Systems & Applications (ICSOS) (pp. 164-170). IEEE.
[14] Ishiyama, T., Kanai, Y., Ohwaki, J., & Mino, M. (2003, October). Impact of a wireless power transmission system using an ultrasonic air transducer for low-power mobile applications. In IEEE Symposium on Ultrasonics, 2003 (Vol. 2, pp. 1368-1371). IEEE.
[15] Kurs, A., Karalis, A., Moffatt, R., Joannopoulos, J. D., Fisher, P., & Soljacic, M. (2007). Wireless power transfer via strongly coupled magnetic resonances. science, 317(5834), 83-86.
[16] Cannon, B. L., Hoburg, J. F., Stancil, D. D., & Goldstein, S. C. (2009). Magnetic resonant coupling as a potential means for wireless power transfer to multiple small receivers. IEEE transactions on power electronics, 24(7), 1819-1825.
[17] Karakaya, U. (2007). Motor Control Via Wireless Energy & Information Transfer, M.Sc. Thesis, Institute of Science & Technology, Istanbul Technical University, Turkiye.
[18] Sample, A. P., Meyer, D. T., & Smith, J. R. (2010). Analysis, experimental results, & range adaptation of magnetically coupled resonators for wireless power transfer. IEEE Transactions on industrial electronics, 58(2), 544-554.
[19] Koma, R., Nakamura, S., Ajisaka, S., & Hashimoto, H. (2011, July). Basic analysis of the circuit model using relay antenna in magnetic resonance coupling position sensing system. In 2011 IEEE/ASME International Conference on Advanced Intelligent Mechatronics (AIM) (pp. 25-30). IEEE.
[20] Cheon, S., Kim, Y. H., Kang, S. Y., Lee, M. L., Lee, J. M., & Zyung, T. (2010). Circuit-model-based analysis of a wireless energy-transfer system via coupled magnetic resonances. IEEE Transactions on Industrial Electronics, 58(7), 2906-2914.
[21] Wang, C. S., Covic, G. A., & Stielau, O. H. (2004). Power transfer capability & bifurcation phenomena of loosely coupled inductive power transfer systems. IEEE transactions on industrial electronics, 51(1), 148-157.
[22] Sallán, J., Villa, J. L., Llombart, A., & Sanz, J. F. (2009). Optimal design of ICPT systems applied to electric vehicle battery charge. IEEE Transactions on Industrial Electronics, 56(6), 2140-2149.
[23] Chopra, S., & Bauer, P. (2011, October). Analysis & design considerations for a contactless power transfer system. In 2011 IEEE 33rd International Telecommunications Energy Conference (INTELEC) (pp. 1-6). IEEE.
[24] Imura, T., & Hori, Y. (2011). Maximizing air gap & efficiency of magnetic resonant coupling for wireless power transfer using equivalent circuit & Neumann formula. IEEE Transactions on industrial electronics, 58(10), 4746-4752.
[25] Jang, Y. J., Suh, E. S., & Kim, J. W. (2015). System architecture & mathematical models of electric transit bus system utilizing wireless power transfer technology. IEEE Systems Journal, 10(2), 495-506.
[26] Low, Z. N., Casanova, J. J., Maier, P. H., Taylor, J. A., Chinga, R. A., & Lin, J. (2009). Method of load/fault detection for loosely coupled planar wireless power transfer system with power delivery tracking. IEEE Transactions on Industrial Electronics, 57(4), 1478-1486.
[27] Jadidian, J., and Katabi, D. (2014). Magnetic MIMO, (495–506).
[28] Agcal, A., Ozcira, S., and Bekiroglu, N. (2016). Wireless power transfer by using magnetically coupled resonators. Journal of Wireless Power Transfer: Fundamentals and Technologies, 49-66.
[29] Ozdemir, C. (2017). Adaptive Control System Design and Implementation for Power Quality and Power Transfer Efficiency at Wireless Power Transfer Systems, M.Sc. Thesis, Institute of Science and Technology, Mersin University, Türkiye.
[30] Jeong, S., Lin, T. H., & Tentzeris, M. M. (2019). A real-time range-adaptive impedance matching utilizing a machine learning strategy based on neural networks for wireless power transfer systems. IEEE Transactions on Microwave Theory & Techniques, 67(12), 5340-5347.
[31] Bai, T., Mei, B., Zhao, L., & Wang, X. (2019). Machine learning-assisted wireless power transfer based on magnetic resonance. IEEE Access, 7, 109454-109459.
[32] Ustun, D., Balci, S., & Sabanci, K. (2020). A parametric simulation of the wireless power transfer with inductive coupling for electric vehicles, & modelling with artificial bee colony algorithm. Measurement, 150, 107082.
[33] Faraci, G., Raciti, A., Rizzo, S. A., & Schembra, G. (2020). Green wireless power transfer system for a drone fleet managed by reinforcement learning in smart industry. Applied Energy, 259, 114204.
[34] Kim, J., Clerckx, B., & Mitcheson, P. D. (2020). Signal & system design for wireless power transfer: Prototype, experiment & validation. IEEE Transactions on Wireless Communications, 19(11), 7453-7469.

[35] Gheisarnejad, M., Farsizadeh, H., Tavana, M. R., & Khooban, M. H. (2020). A novel deep learning controller for DC–DC buck–boost converters in wireless power transfer feeding CPLs. IEEE Transactions on Industrial Electronics, 68(7), 6379-6384.

[36] Nam, I., Dougal, R., & Santi, E. (2012, September). Novel control approach to achieving efficient wireless battery charging for portable electronic devices. In 2012 IEEE Energy Conversion Congress & Exposition (ECCE) (pp. 2482-2491). IEEE.

[37] Phokhaphan, N., Choeisai, K., Noguchi, K., Araki, T., Kusaka, K., Orikawa, K., & Itoh, J. I. (2013, November). Wireless power transfer based on MHz inverter through PCB antenna. In 2013 1st International Future Energy Electronics Conference (IFEEC) (pp. 126-130). IEEE.

[38] Gao, L., Hu, W., Xie, X., Deng, Q., Wu, Z., Zhou, H., & Jiang, Y. (2013, June). Optimum design of coil for wireless energy transmission system based on resonant coupling. In 2013 10th IEEE International Conference on Control & Automation (ICCA) (pp. 190-195). IEEE.

[39] Ahn, D., & Hong, S. (2013). A transmitter or a receiver consisting of two strongly coupled resonators for enhanced resonant coupling in wireless power transfer. IEEE transactions on industrial electronics, 61(3), 1193-1203.

[40] Villar, I., Iruretagoyena, U., Rujas, A., Garcia-Bediaga, A., and de Arenaza, I. P. (2015, September). Design and implementation of a SiC based contactless battery charger for electric vehicles. In 2015 IEEE Energy Conversion Congress & Exposition (ECCE) (pp. 1294-1300). IEEE.

[41] Kuzey, S., Balci, S., & Altin, N. (2017). Design & analysis of a wireless power transfer system with alignment errors for electrical vehicle applications. International journal of hydrogen energy, 42(28), 17928-17939.

[42] Aydin, E., Kosesoy, Y., Yildiriz, E., & Aydemir, M. T. (2018, November). Comparison of hexagonal & square coils for use in wireless charging of electric vehicle battery. In 2018 International Symposium on Electronics & Telecommunications (ISETC) (pp. 1-4). IEEE.

[43] Doğan, Z., Özsoy, M., & İskender, İ. (2019). Manyetik Rezonansa Dayalı Kablosuz Enerji Transferi İçin Yeni Bir Nüve Geometrisi. Gazi University Journal of Science Part C: Design & Technology, 7(4), 1012-1024.

[44] Neves, A., Sousa, D. M., Roque, A., & Terras, J. M. (2011, August). Analysis of an inductive charging system for a commercial electric vehicle. In Proceedings of the 2011 14th European Conference on Power Electronics & Applications (pp. 1-10). IEEE.

[45] Kusaka, K., & Itoh, J. I. (2012, October). Input impedance matched AC-DC converter in wireless power transfer for EV charger. In 2012 15th International Conference on Electrical Machines & Systems (ICEMS) (pp. 1-6). IEEE.

[46] Fincan, B. (2015). Designing A Wireless Charger For Electrical Vehicles, M.Sc. Thesis, Institute of Science & Technology, Istanbul Technical University, Turkiye.

[47] Kuzey, S. (2017). Design of Inductive Magnetic Coupled Power Transmission System for Electric Vehicle, M.Sc. Thesis, Institute of Science & Technology, Gazi University, Turkiye.

[48] Yakala, R. K., Pramanick, S., Nayak, D. P., & Kumar, M. (2021). Optimization of circular coil design for wireless power transfer system in electric vehicle battery charging applications. Transactions of the Indian National Academy of Engineering, 6, 765-774.

[49] Çiçek, M., Gençtürk, M., Balci, S., & Sabanci, K. (2021). The modelling, simulation, & implementation of wireless power transfer for an electric vehicle charging station. Turkish Journal of Engineering, 6(3), 223-229.

[50] Moradewicz, A. J., & Kazmierkowski, M. P. (2009). High efficiency contactless energy transfer system with power electronic resonant converter. Bulletin of the Polish Academy of Sciences: Technical Sciences, 375-381.

[51] Rao¹, T. C., & Geetha, K. (2016). Categories, standards & recent trends in wireless power transfer: A survey. Indian journal of science and technology, 9, 20.

[52] Cicek, M. (2022). Modeling, Simulation and Analysis of Wireless Power Transfer, M.Sc. Thesis, Institute of Science and TechnologyKaramanoglu Mehmetbey University, Turkiye.

[53] Zheng, C. (2015). Loosely Coupled Transformer and Tuning Network Design for High-Efficiency Inductive Power Transfer Systems, Ph.D. Thesis, Virginia Polytechnic Institute and State University. Blacksburg, Virginia.

[54] Khayrudinov, V. (2015). Wireless Power Transfer system : Development and Implementation, B.Sc. Thesis, ResearchGate, Helsinki Metropolia University of Applied Sciences.

[55] Lu, X., Wang, P., Niyato, D., Kim, D. I., and Han, Z. (2015). Wireless charging technologies: Fundamentals, standards, and network applications. IEEE communications surveys and tutorials, 18(2), 1413-1452.

[56] Coca, E. (2016). Wireless Power Transfer - Fundamentals and Technologies.

[57] Cheng, D. K. (1983). Field and Wave Electromagnetics.

[58] Rosa, E. B., & Grover, F. W. (1912). Formulas and tables for the calculation of mutual and self-inductance (Revised). Bulletin of the Bureau of Standards, 8(1), 1.

[59] Uzun, G. (2012). Wireless Energy Transfer, M.Sc. Thesis, Institute of Science and Technology Ondokuz Mayıs University, Turkiye.

[60] Mendes Duarte, R., & Klaric Felic, G. (2014). Analysis of the coupling coefficient in inductive energy transfer systems. Active & Passive Electronic Components.
[61] Liu, X., Xia, C., & Yuan, X. (2018). Study of the circular flat spiral coil structure effect on wireless power transfer system performance. Energies, 11(11), 2875.
[62] Oraz, A. A., & Alkaya, A. (2018). Contacless Power Transfer Methods for Electirc Vehicles Charging, CISET 2018 Cilicia International Symposium on Engineering & Technology, Mersin, Turkiye.
[63] Zhang, Y., Yan, Z., Zhu, J., Li, S., & Mi, C. (2019). A review of foreign object detection (FOD) for inductive power transfer systems, eTransportation, Volume 1, 100002, https://doi.org/10.1016/j.etran.2019.04.002.
[64] Wheeler, H. A. (1928). Simple inductance formulas for radio coils. Proceedings of the institute of Radio Engineers, 16(10), 1398-1400.
[65] Agcal, A. (2017). Design & Implementation of a High Efficiency Wireless Power Transfer System with A New Closed Loop Algorithm, Ph.D. Thesis, Institute of Science & Technology Yıldız Technical University, Turkiye.
[66] Namadmalan, A., Jaafari, B., Iqbal, A., & Al-Hitmi, M. (2020). Design optimization of inductive power transfer systems considering bifurcation & equivalent AC resistance for spiral coils. IEEE Access, 8, 141584-141593.
[67] Fawwaz U. R., & Ulaby, T. (2015). Fundamentals of applied electrostatics.

doi:10.55385/kastamonujes.1301461 KUJES 9(1):33-45, 2023

Kastamonu University
Journal of Engineering and Sciences
e-ISSN 2667-8209
http://dergipark.gov.tr/kastamonujes

Comparison of Absorption-Emission Properties of New Azo Dyes and New Schiff Bases from Benzimidazole Derivative 1,3,4-Thiadiazole and Theoretical Calculation by DFT Method

Nesrin Şener[a, *], Sevil Özkınalı[b], Mahmut Gür[c], Merve Zurnacı[d], İzzet Şener[e], M. Serdar Çavuş[f]

[a] Department of Chemistry, Faculty of Science, Kastamonu University, 37200, Kastamonu, Türkiye
[b] Department of Chemistry, Faculty of Science-Arts, Hitit University, Çorum, Türkiye
[c]Department of Forest Industrial Engineering, Faculty of Forestry, Kastamonu University, 37200, Kastamonu, Türkiye
[d]Institute of Science, Kastamonu University, 37200 Kastamonu, Türkiye
[e]Department of Food Engineering, Faculty of Engineering and Architecture, Kastamonu University, 37200, Kastamonu, Türkiye
[f]Department of Biomedical Engineering, Faculty of Engineering and Architecture, Kastamonu University, Kastamonu, Türkiye
***Corresponding Author:** nsener@kastamonu.edu.tr

Received: **May 23, 23023** ◆ Accepted: **June 14, 2023** ◆ Published Online: **June 21, 2023**

Abstract: After the synthesis of the new benzimidazole derivative 1,3,4-thiadiazole compound, a series of azo dyes from the reaction of this compound with various coupling components and a series of schiff bases were synthesized from the reaction with various aldehydes. The structures of the obtained compounds are characterized and interpreted with UV, FT-IR and ^{1}H-NMR. The fluorescence properties of the compounds were also investigated, and the absorption and emission properties of schiff base and azo dyes obtained from the same derivative were examined. As a result, it was observed that schiff bases obtained from benzimidazole derivative 1,3,4-thiadiazole compound had longer wavelength absorption-emission compared to azo dyes obtained from the same compound. Experimental data were supported by density functional theory (DFT) calculations. The ground state geometries, spectroscopic properties, FMO energies and related chemical reactivity parameters of the compounds were calculated using the B3LYP hybrid density functional combined with 6-311++G(2d,2p) basis set. At the same theory level, QTAIM and IRI analyzes were also performed and the data were used to determine the properties of tautomeric structures. The electronic properties of the compounds were studied and a detailed analysis was performed by comparing them with experimental data.

Keywords: Benzimidazole, Azo dyes, Schiff bases, Fluorescence, Absorption properties, DFT method

Öz: Yeni benzimidazol türevi 1,3,4-tiyadiazol bileşiğinin sentezinden sonra, bu bileşiğin çeşitli kenetleme bileşenleriyle reaksiyonundan bir dizi azo boya ve çeşitli aldehitlerle reaksiyonundan bir dizi schiff bazı sentezlenmiştir. Elde edilen bileşiklerin yapıları UV-Vis., FT-IR ve ^{1}H-NMR ile karakterize edilerek yorumlanmıştır. Bileşiklerin floresans özellikleri de araştırılmış, aynı türevden elde edilen schiff bazı ve azo boyaların absorpsiyon ve emisyon özellikleri de incelenmiştir. Sonuç olarak, benzimidazol türevi 1,3,4-tiyadiazol bileşiğinden elde edilen schiff bazlarının, aynı bileşikten elde edilen azo boyalara göre daha uzun dalga boyunda absorpsiyon-emisyona sahip olduğu gözlendi. Deneysel veriler, yoğunluk fonksiyonel teorisi (DFT) hesaplamaları ile desteklenmiştir. Bileşiklerin temel durum geometrileri, spektroskopik özellikleri, FMO enerjileri ve ilgili kimyasal reaktivite parametreleri, 6-311++G(2d,2p) temel seti ile birleştirilmiş B3LYP hibrit yoğunluk fonksiyoneli kullanılarak hesaplanmıştır. Aynı teori seviyesinde QTAIM ve IRI analizleri de yapılmış ve veriler tautomerik yapıların özelliklerini belirlemede kullanılmıştır. Bileşiklerin elektronik özellikleri incelenmiş ve deneysel verilerle karşılaştırılarak detaylı analiz yapılmıştır.

Anahtar Kelimeler: Benzimidazol, Azo boyalar, Schiff bazları, Floresans, Absorpsiyon özellikleri, DFT yöntemi

1. Introduction

Benzimidazoles are one of the most important *N*-containing organic compounds in a wide variety of natural products and pharmaceuticals [1,2]. Despite numerous attempts to develop new structural prototypes in the search for more effective antimicrobials, benzimidazoles continue to remain a versatile compound against microorganisms [3-10] and therefore, they are useful sub-structures for further molecular investigations. On the other hand, it has been shown in the literature that 1,3,4-thiadiazoles are also associated with pharmacological activities such as antimicrobial, antiviral, anesthetic and anticonvulsant [11-15]. Although not many, there are benzimidazole derivative 1,3,4-thiadiazole compounds in previous studies [16,17]. Similarly, antimicrobial activity studies of these compounds have been conducted.

Fluorescence property of molecules is a biologically important method due to its high sensitivity [18-21]. It is known that fluorescence spectroscopy has a wide application in both analytical and diagnostic studies as a very sensitive and informative method for the characterization of simple and complex molecules [22]. Therefore, it is very important to

study the absorption and emissions of organic molecules such as azo dyes and schiff bases, which are important in terms of their biological properties and have been studied by researchers. Fluorescent dyes are characterized by extraordinarily bright colors, as they not only absorb but also emit in the visibility [23, 24]. Fluorescent dyes are used for various applications, such as for a solid-state dye laser system [25], polymer treatment [26], optical fibres [27] and solid-state dye-labelled DNA [28] to detect volatile compounds in the vapor phase. It is possible to talk about similar fluorescent properties for Schiff bases. For example, while in a study a simple Schiff base (*Z*)-*N*-benzylidene naphthalen-1-amine (L) acts as an effective fluorescence sensor for Al^{+3} [29], in another study, a turn-on Schiff base for the Zinc ion is mentioned [30]. In a study, Guo synthesized some schiff-base macromolecular ligand by copolymerizing schff-base monomer, methyl methacrylate and ethyl acrylate. After preparation of the polymeric materials based on terbium complex with this macromolecular ligand, the fluorescence properties of the terbium-complex polymer were investigated experimentally [31].

In present study, in the first step, we obtained 1,3,4-thiadiazole derivative from the reaction of benzimidazole-5-carboxylic acid and thiosemicarbazide. In the next step, we synthesized five different azo dyes and five different schiff bases from this 1,3,4-thiadiazole derivative. These compounds obtained after the experimental stage were characterized by spectroscopic methods such as ^{1}H-NMR and FT-IR. Then, the absorption and emission measurements of these synthesis compounds were examined and discussed. In addition, DFT calculations were performed for a theoretical analysis of experimental results. Electronic parameters such as highest occupied molecular orbital (HOMO), lowest unoccupied molecular orbital (LUMO) energies, electronegativity (χ), chemical hardness (η), and polarizability (α), electrophilic index (ω), nucleophilic index (**ε**), electrodonating power (ω^-) were calculated at the B3LYP/6-311++G(2d,2p) level of theory. FT-IR, UV-Vis and ^{1}H-NMR spectra of the compounds were obtained using the same method and basis set. The relationship between tautomeric transitions and electronic properties of compounds was investigated theoretically.

2. Material and Method

Benzophenone-4,4'-dicarboxylic acid was purchased from TCI chemicals whereas phosphorous oxychloride (99%) was from Merck. Thiosemicarbazide was provided from Sigma-Aldrich, ethanol solvent was bought from Tekkim Company. Melting points were taken with Stuart SMP10 apparatus. UV-Vis. absorption spectra were recorded with Shimadzu UV Mini-1240 UV-Vis. spectrophotometer by using cyclohexanone, DMF, 1,4-dioxane and DMSO (by Merck) as solvent. FT-IR spectra were taken in the region 400-4000 cm^{-1} on Alpha FTIR spectrometer Bruker. The ^{1}H-NMR spectra were recorded on Bruker AVANCE III 400 MHz NMR spectrophotometer at room temperature in dimethyl sulfoxide-d_6 (DMSO-d_6). The photoluminescence (PL) spectra were recorded in a 1 cm path length quartz cell using a Horiba FluoroMax-4 fluorescence spectrometer.

Synthesis of compound 1

Benzimidazole carboxylic acid compound (n mol), thiosemicarbazide (n mol) and $POCl_3$ (3 mol) were placed in a 100 mL flask and refluxed for 3 hours at 90 °C, cooled, 50 mL of cold water was added and mixed, then filtered. The filtrate was neutralized with 25% aqueous NH_3. The precipitate formed was separated by filtration. It was washed with water, dried and purified (compound 1). The yield was calculated by weighing the dried sample. The melting point was checked. Final product; FT-IR, ^{1}H-NMR. Yield: 72% m.p 295 °C. IR ν (cm^{-1}) = 3250 (-NH_2), 3113 (-NH), 3021 (C-$H_{arom.}$), 1643 (-CH=N-), 1622 (-C=C-), 708 (-C-S-C-).^{1}H-NMR (d_6-DMSO, ppm): δ= 7,35 (s, 2H, -NH_2), 7,90-8,66 (aromatic C-H), 8,53 (s,-NH); The synthesis reaction pattern is shown in Figure 1.

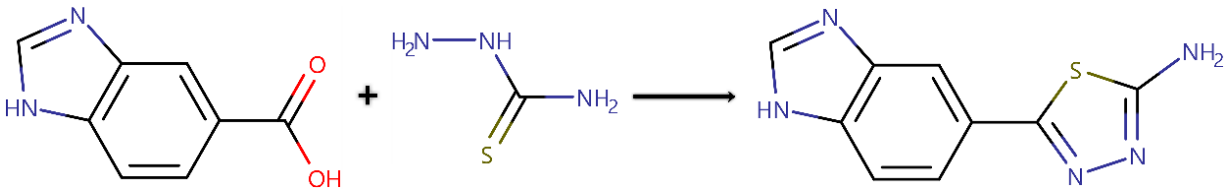

Figure 1. Synthesis reaction of compound 1.

General Synthesis Method of Compound 2(a-e)

Obtained benzimidazole derivative 1,3,4-thiadiazole compound (Compound 1) (n mol) is dissolved in HCl (3 mL) and acetic acid (6 mL), and added $NaNO_2$, which is dissolved in sulfuric acid at the minimum rate, mixed in the range of 0-5 ^oC to prepare the diazonium salt. After two hours, it was stirred at 0-5 °C for 2 hours with the addition of various coupling compounds (n mol) in basic medium. As a result of the coupling reaction, five different azo dyes were synthesized. The synthesis reaction pattern is shown in Figure 2.

(*E*)-3-((5-(1*H*-benzo[d]imidazol-5-yl)-1,3,4-thiadiazol-2-yl)diazenyl)-4-hydroxyquinolin-2(3H)-one (Compound 2a)
Yield: 62% m.p 340 °C. IR ν (cm^{-1}) = 3256 (-OH), 3154 (-NH), 3092 (C-$H_{arom.}$), 1658 (C=O), 1630 (C=C), 1606 (-C=N-), 1564-1469 (N=N), 723 (-C-S-C-).^{1}H-NMR (DMSO-d_6, ppm): δ= 5.71 (1H, s, benzimidazole -NH), 7.07-7,83 (8H, aromatic C-H),), 11.17 ve 11.28 (2H, s, -OH).

(*E*)-2-((5-(1*H*-benzo[d]imidazol-5-yl)-1,3,4-thiadiazol-2-yl)diazenyl)naphthalen-1-ol (Compound 2b)
Yield: 71% m.p 260 °C. IR ν (cm^{-1}) = 3283 (-OH), 3167 (-NH), 3092 (C-$H_{arom.}$), 1620 (-C=C-), 1548-1409 (N=N), 1101 (C-O), 691 (-C-S-C-).^{1}H-NMR (DMSO-d_6, ppm): δ=7.33-8.49 (10H, aromatic C-H), 10.07 (1H, s, -OH).

(*E*)-3-((5-(1*H*-benzo[d]imidazol-5-yl)-1,3,4-thiadiazol-2-yl)diazenyl)-4-hydroxy-2H-chromen-2-one (Compound 2c)
Yield: 61% m.p 290 °C. IR ν (cm^{-1}) = 3342 (-OH), 3209 (-NH), 3093 (C-H_{arom}), 1682 (C=O), 1615 (-C=C-), 1599 (-C=N-), 1516-1448 (N=N), 1051 (C-O), 734 (C-S-C). ^{1}H-NMR (400 MHz, DMSO-d_6) δ (ppm): 5.60 (1H, s, benzimidazole -NH), 7.32-8,00 (8H, aromatic C-H), 8.42 (1H, s, -OH).

(*E*)-4-((5-(1*H*-benzo[d]imidazol-5-yl)-1,3,4-thiadiazol-2-yl)diazenyl)-3-methyl-1H-pyrazol-5-ol (Compound 2d)
Yield: 67% m.p 315 °C. IR ν (cm^{-1}) = 3271 (-OH), 3115 (-NH), 3094 (C-H_{arom}), 2988 (C-$H_{aliphatic}$), 1614 (-C=C-), 1545-1449 (N=N), 1036 (C-O), 769 (C-S-C). ^{1}H-NMR (400 MHz, DMSO-d_6) δ (ppm): 2.50 (3H, s, -CH_3), 4.83 (1H, s, benzimidazole -NH), 7.39-8,12 (4H, aromatic C-H), 8.91 (1H, s, pyrazole -NH).

(*E*)-4-((5-(1*H*-benzo[d]imidazol-5-yl)-1,3,4-thiadiazol-2-yl)diazenyl)-3-methyl-1-phenyl-1H-pyrazol-5-ol (Compound 2e)
Yield: 68% m.p 310 °C. IR ν (cm^{-1}) = 3272 (-OH), 3112 (-NH), 3092 (C-H_{arom}), 2913 (C-$H_{aliphatic}$), 1613 (C=C), 1546-1449 (N=N), 689 (C-S-C). ^{1}H-NMR (400 MHz, $CDCl_3$) δ (ppm): 2.51 (3H, s, -CH_3), 5.93 (1H, s, benzimidazole -NH), 7.37-8,05 (9H, aromatic C-H), 8.87 (1H, -OH).

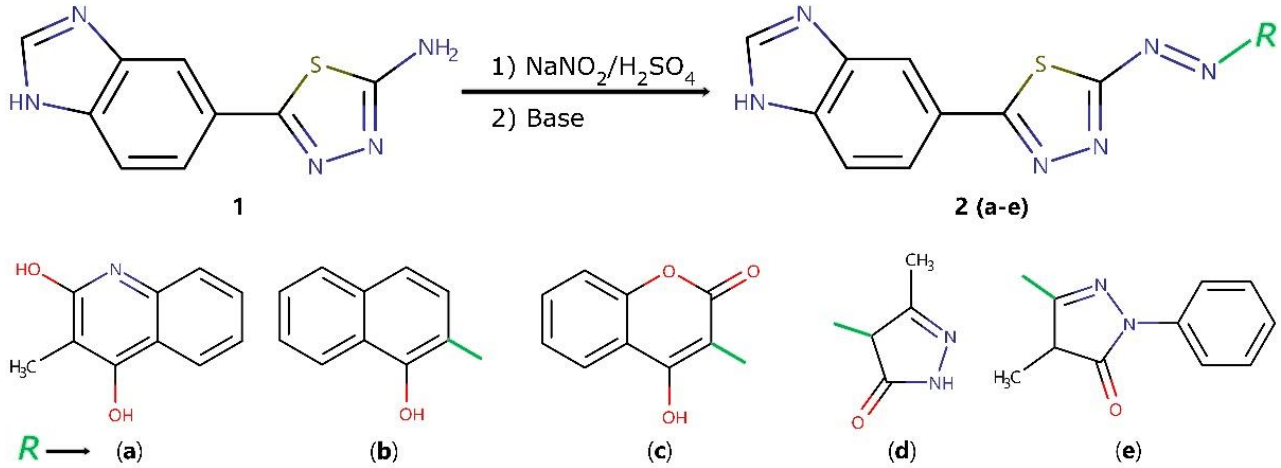

Figure 2. Synthesis reaction of compound 2(a-e).

General Synthesis Method of Compound 3(a-e)

The obtained compound 1 was reacted with various aldehydes in ethanol (50 mL) at a ratio of 1:1 in reflux for 24 hours, and the precipitates formed in the reaction chamber were filtered and crystallized. Afterwards, structural analysis of these five different schiff base derivatives was performed with different spectroscopic methods. The synthesis reaction pattern is shown in Figure 3.

(*E*)-5-(1*H*-benzo[d]imidazol-5-yl)-*N*-(4-methoxybenzylidene)-1,3,4-thiadiazol-2-amine (Compound 3a)
Yield: 74% m.p 285 °C. IR ν (cm^{-1}) = 3121 (-NH), 3039 (C-H_{arom}), 2918-2824 (C-$H_{aliphatic}$), 1665 (N=CH), 1622 (C=C), 1099 (C-O), 730 (C-S-C). ^{1}H-NMR (400 MHz, DMSO-d_6) δ (ppm): 3.43 (3H, s, -OCH_3), 7.31 (1H,s, -NH), 7.63-8,46 (8H, aromatic C-H), 8.53 (1H, s,-N=CH).

(*E*)-4-(((5-(1*H*-benzo[d]imidazol-5-yl)-1,3,4-thiadiazol-2-yl)imino)methyl)phenol (Compound 3b)
Yield: 75% m.p 280 °C. IR ν (cm^{-1}) = 3351 (-OH), 3186 (-NH), 3048 (C-H_{arom}), 2912 (C-$H_{aliphatic}$), 1652 (N=CH), 1624 (C=C), 1594 (C=N), 1108 (C-O), 730 (C-S-C). ^{1}H-NMR (400 MHz, DMSO-d_6) δ (ppm): 6.96 (1H, s, -NH), 7.30-8.47 (8H, aromatic C-H), 8.91 (1H, s, N=CH), 10.63 (1H, s, -OH).

(*E*)-5-(1*H*-benzo[d]imidazol-5-yl)-*N*-(4-chlorobenzylidene)-1,3,4-thiadiazol-2-amine (Compound 3c)
Yield: 71% m.p 280 °C. IR ν (cm^{-1}) = 3122 (-NH), 3065 (C-H_{arom}), 2921 (C-$H_{aliphatic}$), 1653 (-N=CH), 1622 (C=C), 738 (C-S-C). ^{1}H-NMR (400 MHz, DMSO-d_6) δ (ppm): 7.33 (1H, s, -NH), 7.72-8,48 (8H, aromatic C-H), 8.53 (1H, s, -N=CH).

(*E*)-5-(1*H*-benzo[d]imidazol-5-yl)-*N*-(4-nitrobenzylidene)-1,3,4-thiadiazol-2-amine (Compound 3d)

Yield: 74% m.p 220 °C. IR ν (cm^{-1}) = 3113 (-NH), 3083 (C-H_{arom}), 2965 (C-$H_{aliphatic}$), 1648 (N=CH), 1624 (C=C), 1557 (-NO_2), 729 (C-S-C). ^{1}H-NMR (400 MHz, DMSO-d_6) δ (ppm): 7.32 (1H, s, -NH), 7.62-8,06 (8H, aromatic C-H), 10.17 (1H, s, N=CH).

(*E*)-5-(1*H*-benzo[d]imidazol-5-yl)-*N*-(4-fluorobenzylidene)-1,3,4-thiadiazol-2-amine (Compound 3e)

Yield: 73% m.p 275 °C. IR ν (cm^{-1}) = 3139 (-NH), 3096 (C-H_{arom}), 2907 (C-$H_{aliphatic}$), 1652 (N=CH), 1623 (C=C), 732 (C-S-C). ^{1}H-NMR (400 MHz, DMSO-d_6) δ (ppm): 7.34 (1H, s, NH), 7.63-8,46 (8H, aromatic C-H), 8.53 (1H, s, -N=CH).

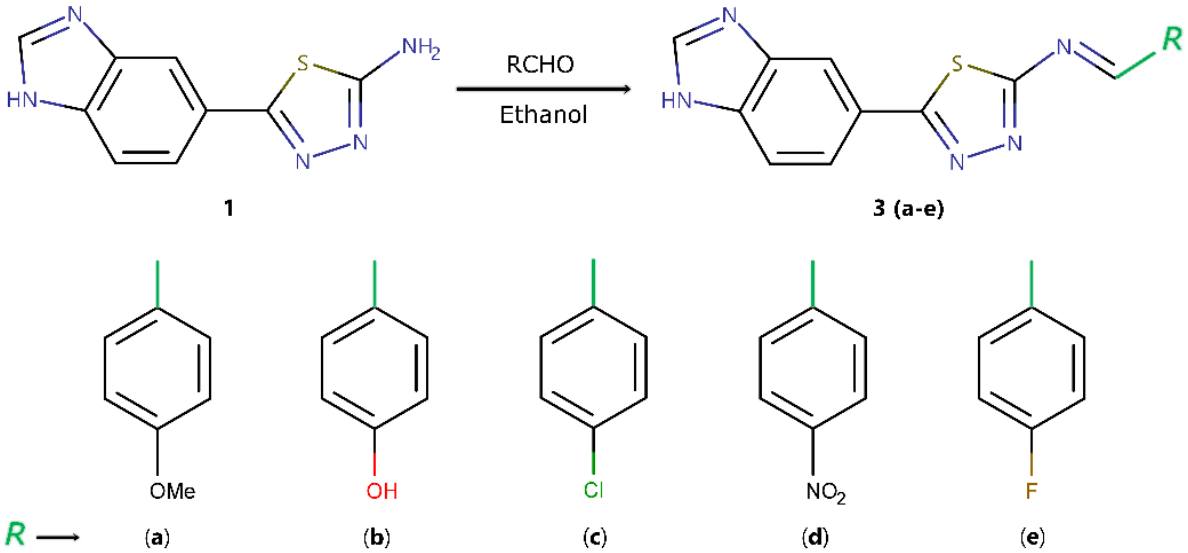

Figure 3. Synthesis reaction of compound 3(a-e).

Absorption and Emission Study

The absorption and emission studies were determined using UV-Vis. (Shimadzu) and fluorescence spectroscopy (Horiba, Fluoromax-3). The absorption and fluorescence emission spectra were studied in DMF and DMSO of all the compounds (concentration of 1×10^{-5} M). The maximum absorption, maximum emission wavelength and Stokes shift are listed in Table 3 for all the compounds.

Computational procedure

First, the compounds were scanned dihedrally using the B3LYP/6-31G theoretical approach to determine the minimum energy conformations (Figure 4). The minimum energy conformations obtained from the dihedral scan were used as input data for all other calculations. All DFT [32, 33] calculations were performed using Gaussian 09 software [34], using B3LYP/6-311++G(2d,2p) level of theory. The optimized state geometries correspond to the global minimum energy points on the potential energy surface, so no imaginary frequencies were observed in the IR calculations performed in the gas phase.

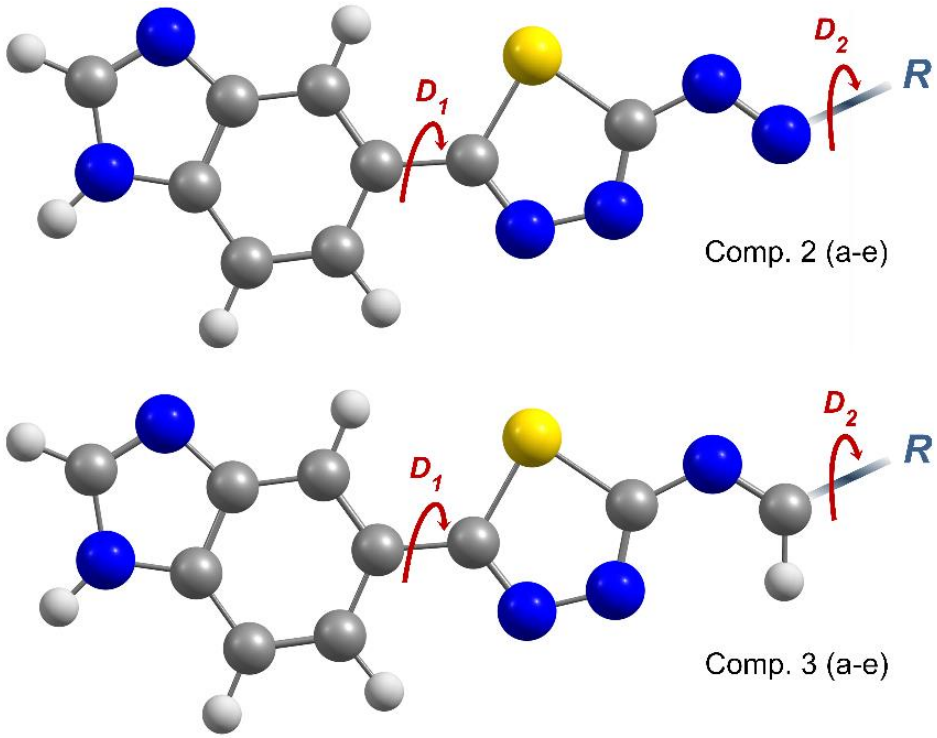

Figure 4. Dihedral scanning of the compounds 2(a-e) and 3(a-e) by 360 steps with a 20-degree rotations D_1 and D_2.

In parallel with the acquisition of experimental NMR data in dimethyl sulfoxide (DMSO) solvent, DFT/^{1}H-NMR calculations were also performed in the DMSO phase using Gauge-independent atomic orbital (GIAO) method, and conductor-like polarizable continuum model (CPCM) was used for solution–solvent interaction in these processes. Relative chemical shift values were calculated by subtracting the absolute chemical shielding of tetramethylsilane (TMS) performed at the B3LYP/6-311++G(2d,2p) level (31,8149 ppm for ^{1}H-NMR).

The IR calculations were performed in the gas phase and the electronic parameters of the compounds were also obtained from the gas phase calculations. Global chemical reactivity parameters such as HOMO-LOMO energy gap ($\boldsymbol{E_g}$), chemical hardness (η), electronegativity (χ), electrophilic index (ω), nucleophilic index ($\boldsymbol{\varepsilon}$), and electrodonating power indices (ω^-) were calculated using frontier molecular orbital (FMO) energy eigenvalues obtained from IR calculations.

The electron density on the ring critical points (RCPs) and bond critical points (BCPs) of the compounds was determined using the QTAIM approach [35, 36]. Also, using Multiwfn software [37], interaction region indicator (IRI) calculations were performed to visualize intramolecular interactions.

3. Result and Discussion

The reaction procedures of the synthesized compounds were carried out as shown in Figure 1 and Figure 2. Based on the benzophenone-4,4-dicarboxylic acid compound, five new azo dyes and five new Schiff bases were obtained with 61-75% efficiency. Spectroscopic methods such as ^{1}H-NMR and FT-IR were used to characterize the structures of the synthesized compounds.

When we look at the FT-IR spectrum results (in Table 1), we see –OH stretching vibrations of the compounds in the range of 3351-3271 cm^{-1}. We see the bands resulting from –NH stretching vibrations in the structures in the range of 3209-3113 cm^{-1}. While we observe aromatic –CH stretching vibrations in the molecules in the range of 3094-3039 cm^{-1}, we observe aliphatic –CH stretching vibrations in the range of 2965-2824 cm^{-1}. The C=O stretching vibration bands observed for compounds 2a and 2c are 1658 and 1682 cm^{-1}, respectively. N=CH stretching vibrations of compounds 3(a-e) are observed in the range of 1665-1648 cm^{-1}. In generally, the C=C stretching vibrations of the compounds are observed in the range of 1630-1613 cm^{-1}, while the bands of the C=N stretching vibrations are observed in the range of 1606-1599 cm^{-1}. The stretching and bending vibrations of azo bridges with compound 2(a-e) are observed in the range of 1564-1516 cm^{-1} and 1469-1409 cm^{-1}, respectively. The stretching vibrations of the C–O bonds in the molecular structures were observed in the range of 1108-1036 cm^{-1}. The bands of stretching vibrations of C–S–C bonds in all compounds obtained were seen in the range of 732-689 cm^{-1}.

Table 1. Experimental and theoretical FT-IR spectrum results of the compounds (cm^{-1}). (Scaling factors: 0.901 for –OH, 0.861 for –NH, 0.963 for C–H (Ar.), 0.948 for C–H (Alip.), 0.937 for C-S-C)

	Com.	$\upsilon_{(-OH)}$	$\upsilon_{(-NH)}$	$\upsilon_{C-H\ (Ar.)}$	$\upsilon_{C-H\ (Alip.)}$	$\upsilon_{C=O}$	$\upsilon_{N=CH}$	$\upsilon_{C=N\ thiadiazol}$	$\upsilon_{(NO2)}$	$\upsilon_{(N=N)}$	$\upsilon_{(C-O)}$	υ_{C-S-C}
Experimental	**2a**	3256	3154	3092	-	1658	-	1606	-	1564,1469	-	723
	2b	3283	3167	3092	-	-	-	-	-	1548, 1409	1101	691
	2c	3342	3209	3093	-	1682	-	1599	-	1516, 1448	1051	734
	2d	3271	3115	3094	2988	-	-	-	-	1545, 1449	1036	769
	2e	3272	3212	3092	2913	-	-	-	-	1546, 1449	-	689
	3a	-	3121	3039	2918, 2824	-	1665	-	-	-	1099	730
	3b	3351	3186	3048	2912	-	1652	-	-	-	1108	730
	3c	-	3122	3065	2921	-	1653	-	-	-	-	738
	3d	-	3113	3083	2965	-	1648	-	1557, 1448	-	-	729
	3e	-	3139	3096	2907	-	1652	-	-	-	-	732
Calculated	**2a-T**	**3301**	**3152**	**3100-3058**	-	**1766**	-	**1435, 1383**	-	**1570**	-	**726**
	2b	**3245**	**3153**	**3099-3064**	-	-	-	**1424, 1380**	-	**1481**	**1221**	**725**
	2c	**3131**	**3153**	**3099-3067**	-	**1712**	-	**1431, 1381**	-	**1511**	**1124**	**726**
	2d-T	**3333**	**3163, 3155**	**3099-3066**	**2968-2883**	-	-	**1432, 1390**	-	**1491**	**1112**	**726**
	2e-T	**3300**	**3158**	**3099-3066**	**2969-2883**	-	-	**1430, 1382**	-	**1487**	**1091**	**729**
	3a	-	**3153**	**3098-3056**	**2910**	-	**1624**	**1448, 1425**	-	-	**1052**	**729**
	3b	**3449**	**3155**	**3098-3042**	**2912**	-	**1629**	**1450, 1425**	-	-	**1290**	**735**
	3c	-	**3154**	**3098-3059**	**2915**	-	**1649**	**1452, 1421**	-	-	-	**720**
	3d	-	**3154**	**3099-3067**	**2921**	-	**1652**	**1450, 1398**	**1562, 1363**	-	-	**718**
	3e	-	**3153**	**3098-3061**	**2913**	-	**1654**	**1455, 1422**	-	-	-	**732**

2(a-e)-T: Expresses the values of the tautomeric form of the compounds.

When we look at the ^{1}H-NMR spectrum results (in Table 2), we see the peaks of aliphatic protons in the range of 2.50-3.43 ppm, and the aromatic peaks in the range of 7.07-8.49 ppm. While we see the peaks of –*N*H protons in the range of 5.71-8.91 ppm, we see the peaks of –*O*H protons in the range of 8.42-11.28 ppm. We observe the peaks of *N=C*H protons in Schiff base compounds in the range of 8.53-10.17 ppm. In addition, all the peaks of the compounds are compatible with the integration rates.

Table 2. Experimental and theoretical ^{1}H-NMR spectrum results of the compounds (ppm).

	Comp.	***Aliphatic*-H**	***Aromatic*-H**	***N*-H**	***O*-H**	***N=C*-H**
Experimental	**2a**	-	7.83-7.07	5.71	11.17, 11.28	-
	2b	-	8.49-7.33	-	10.07	-
	2c	-	8.00-7.32	5.60	8.42	-
	2d	2.50 (3H, s, $-CH_3$)	8.12-7.39	8.91	-	-
	2e	2.51(3H, s, $-CH_3$)	8.05-7.37	5.93	8.87	-
	3a	3.43 (3H, s, $-OCH_3$)	8.46-7.63	-	-	8.53
	3b	-	8.47-7.30	6.96	10.63	8.91
	3c	-	8.48-7.72	7.33	-	8.53
	3d	-	8.06-7.62	7.32	-	10.17
	3e	-	8.46-7.63	7.34	-	8.53
Calculated	**2a**	-	8.94-7.85	9.50	15.06, 9.11	-
	2b	-	8.97-7.81	9.47	9.91	-
	2c	-	8.93-7.98	9.48	10.76	-
	2d	2.33-2.07 ($-CH_3$)	8.91-5.12	9.50, 8.26	-	-
	2e-T	2.70-2.51 ($-CH_3$)	8.89-7.87	9.46	7.92	-
	3a	4.25-4.02 ($-OCH_3$)	8.85-7.42	9.43	-	9.31
	3b	-	8.81-7.28	9.43	5.55	9.30
	3c	-	8.83-7.94	9.44	-	9.41
	3d	-	9.01-7.99	9.45	-	9.61
	3e	-	8.86-7.65	9.44	-	9.40

The maximum absorption, maximum emission wavelength and Stokes shift are listed in Table 3 for all the compounds. Absorption and emission properties of the compounds changed with solvents. Absorption and emission bands were observed at between 264-321 nm and 324-339 nm, respectively. When comparing the absorption and emission bands of all compounds; it was observed that the wavelengths of compounds in DMSO were higher than DMF. The compound with the highest maximum Stokes shift in DMSO was determined as 2c. The calculated UV absorption rates are given in Figure 5 and it was observed to be in agreement with the experimental results.

The structure of the compounds has been to cause a change in fluorescence emission properties. The maximum fluorescence emission wavelength was determined as the compounds bearing -OH, C=O and –O– (2a, 2c and 3b). At the same time, the Stokes shift of the compounds including –OH, C=O and –O– (in aromatic ring) bond was wider when compared to the other compounds. These compounds contribute to the delocalization due to the electron-donating and activator properties of the –OH, C=O and –O– groups.

Table 3. Absorption-emission properties of the compounds in different solvents (nm)

Comp.	Solvent	Absorbance (nm) λ_{max}	Emission (nm) λ_{max}	Stokes' shift (nm)
2a	DMF	321	439	118
	DMSO	271,281,321,338	439	119
2b	DMF	316	424	108
	DMSO	317	435	118
2c	DMF	308	434	126
	DMSO	264,282,308,320	439	131
2d	DMF	317	427	110
	DMSO	319	436	117
2e	DMF	319	432	113
	DMSO	318	437	119
3a	DMF	314	430	116
	DMSO	316	435	119
3b	DMF	316	423	107
	DMSO	319	438	119
3c	DMF	307	430	123
	DMSO	311	437	126
3d	DMF	315	428	113
	DMSO	318	436	118
3e	DMF	320	424	104
	DMSO	321	435	114

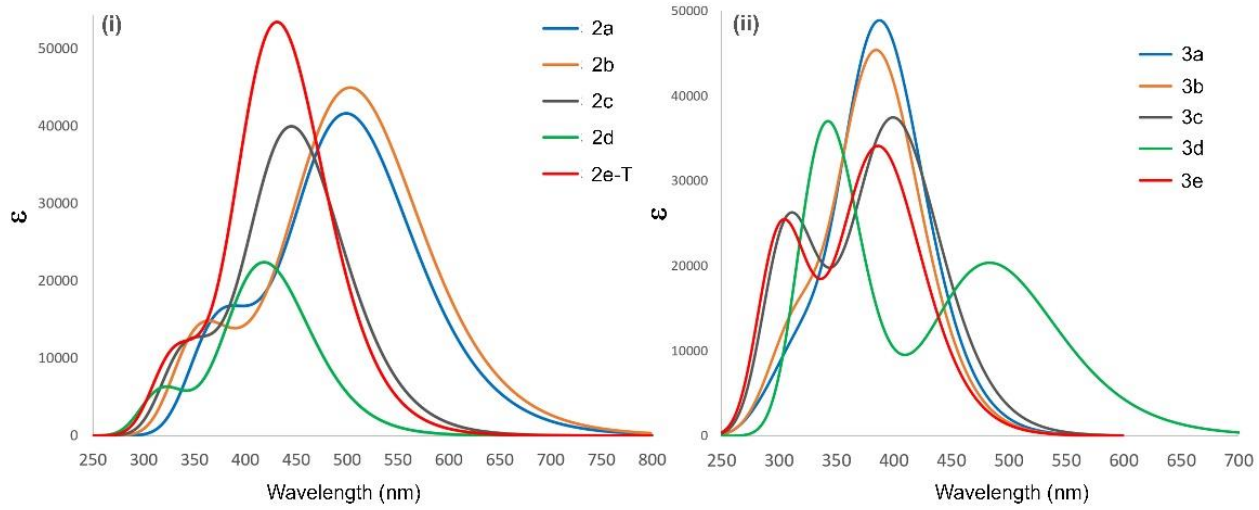

Figure 5. Calculated UV-Vis. absorption peaks of the compounds.

Computational results

Although global chemical reactivity parameters (GCRPs) such as HOMO-LUMO energy gap, electronegativity, chemical hardness, etc. [38, 39], give clues about some basic properties and behaviors of molecular structures, these calculated properties of single molecules (independent of environmental effects, without atomic or molecular pollution) are can not meet the variable electronic properties of molecular structures. In other words, GCRPs can be used to predict how a compound will propensity for any given reaction, but the dependence of a reaction on macro variables such as temperature as well as electronic variables such as the interaction of molecules with the environment and intramolecular interactions makes it difficult to interpret GCRPs calculated on a single molecule structure. However, the ability of the reactions to repeat themselves in experiments with approximately the same results reveals that the relevant reaction is driven by some dominant variables. Thus, it can be said that one or more of the GCRPs may overlap with experimental data in some cases. Starting from this point, some GCRPs of first group 2(a-e) and second group 3(a-e) compounds were calculated and possible reaction characteristics of these compounds were determined (The all values of the calculated GCRPs are given in the Supplementary Table S1).

Calculations for the tautomers of the compounds, which are compounds 2a, 2d, 2e and 2a-T, 2d-T, 2e-T, did not reveal sufficient results to predict a correlation between the total electronic energy and the tautomeric conformational preference. In other words, the data are not sufficient to make the assumption that a lower energy tautomer can be observed more frequently in experiments. However, the HOMO-LUMO energy gap E_g was calculated to be lower in tautomers (2a, 2d, and 2e-T) with intramolecular interacting hydrogens (Figure 5-c). At this point, it can be said that these tautomers have higher chemical reactivity and lower kinetic stability. The results reveal that it is difficult to say that HOMO or LUMO energies are directly related to the characteristics of tautomer structures (see Figure 5-b).

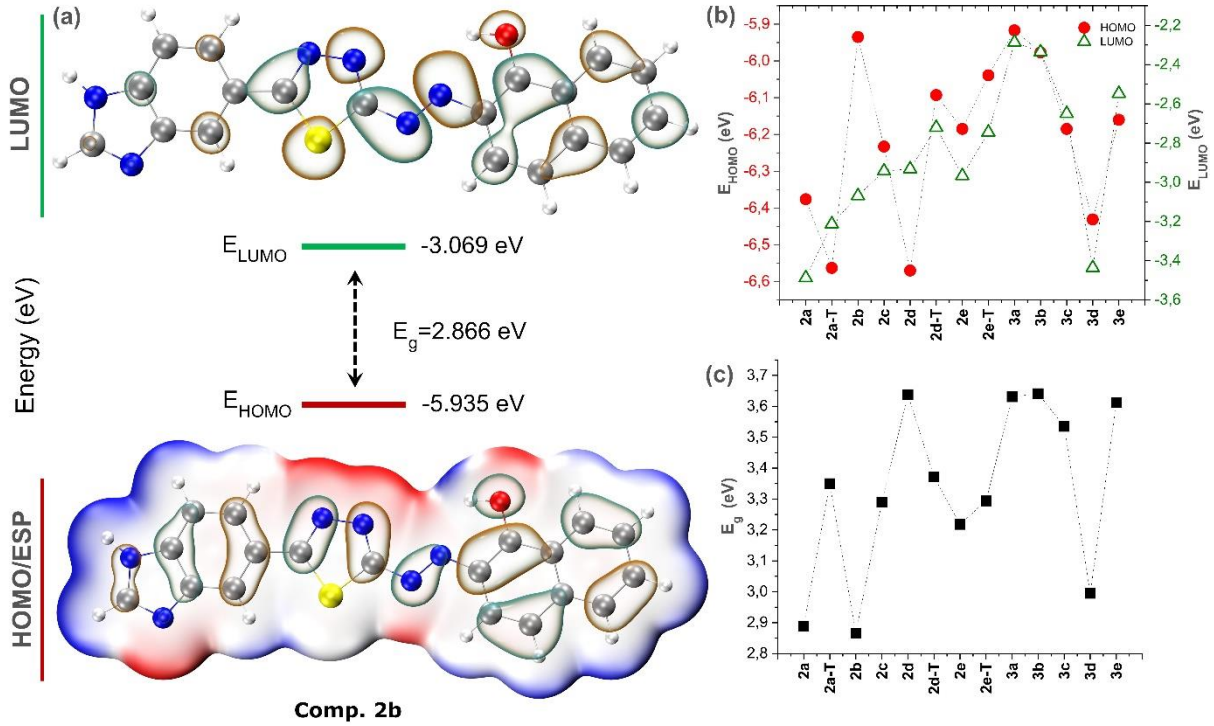

Figure 5. HOMO/ESP and LUMO surfaces (a), HOMO and LUMO energy eigenvalues (b), and HOMO-LUMO energy gap (c) of the compound 2b.

The electronegativity, electrophilic index, and electrodonating power parameters related to the electron affinities of the compounds (Figure 6), reveal that the second group compounds may show higher nucleophilic behavior than the first group compounds, except NO_2 substituted 3d. In addition, both electrophilic indexes and electrodonating power values of tautomers structures 2a-T, 2d-T, and 2e-T were calculated. These results strengthen the conclusion that the synthesis mechanism of the compounds leads them to become nucleophilic. At this point, it should be noted that since the conformations of the tautomers structures selected for the calculations directly affect the calculation results, precise interpretations of the present results cannot be made easily.

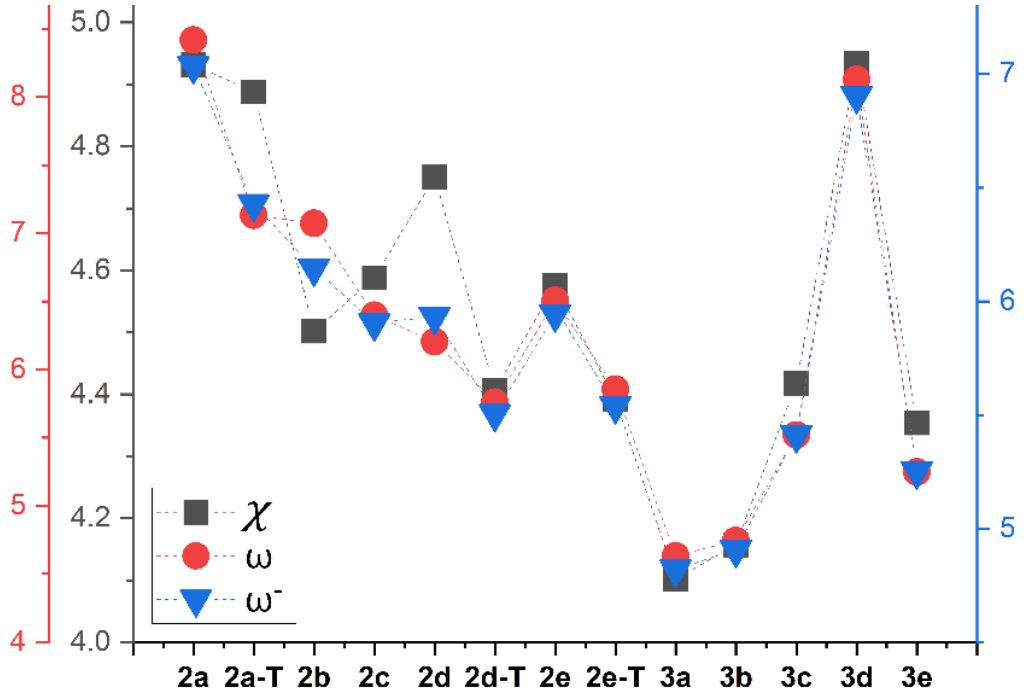

Figure 6. Electronegativity, χ (eV), electrophilic index, ω (eV), and electrodonating power, ω^- (eV) values of the compounds.

IRI and QTAIM calculations were performed to analyze intramolecular interactions and electron charge distributions. Intramolecular interactions for tautomers 2a and 2a-T and IRI surface maps of the intensities of these interactions are in Figure 7, and the calculated charge densities in BCP and RCP are given in Table 4 (see Supplementary Figure S1 for IRI maps of the compounds). The variation of the electron density of the structure to which the hydrogen atom causing the tautomer is attached is quite evident for both visual (for IRI) and calculated values (for QTAIM) on R4 and B(3-7). In addition, although the substituted groups and the structures attached to these groups changed, it was observed that the electron density in the RCPs of these rings changed less than in other RCPs due to the high pi conjugation on the phenyl rings.

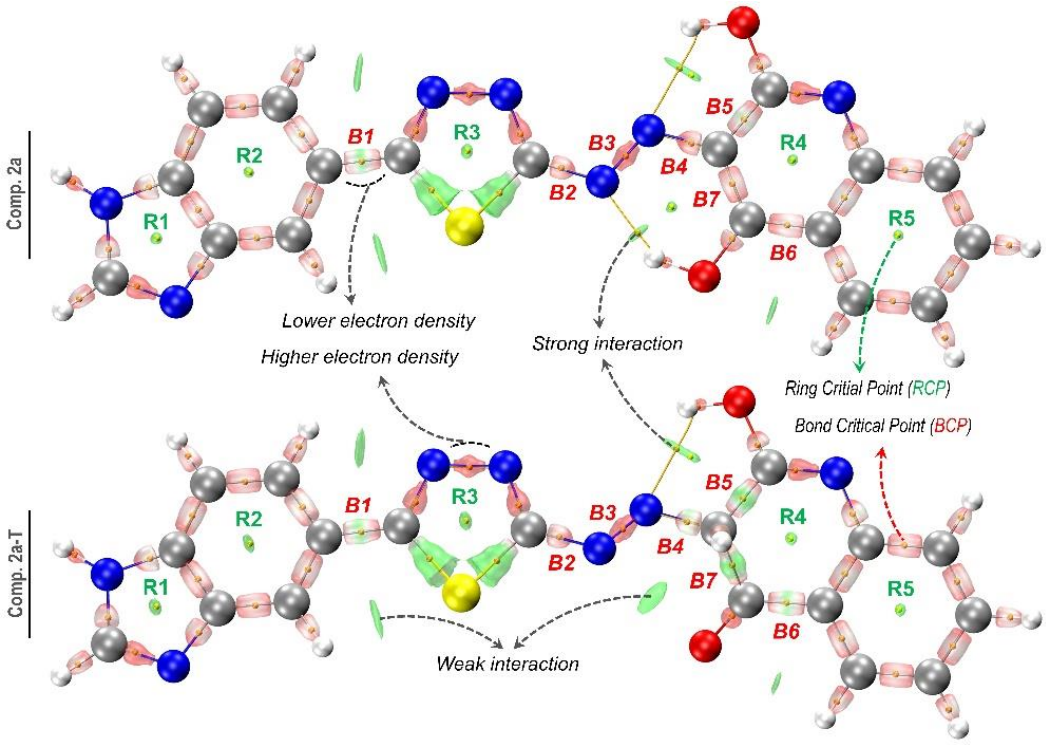

Figure 7. IRI maps and QTAIM data of compounds 2a and 2a-T.

Table 4. Calculated electron charge density of compounds in selected BCPs and RCPs, (*e*/bohr^3)

	2a	2a-T	2b	2c	2d	2d-T	2e	2e-T	3a	3b	3c	3d	3e
R1	0.057196	0.057203	0.057161	0.057166	0.057189	0.057152	0.057192	0.057162	0.057126	0.057130	0.057150	0.057175	0.057147
R2	0.022633	0.022637	0.022637	0.022638	0.022639	0.022639	0.022639	0.022635	0.022642	0.022643	0.022641	0.022638	0.022642
R3	0.046583	0.047008	0.046548	0.046706	0.046932	0.046495	0.046936	0.046414	0.045980	0.046004	0.046122	0.046253	0.046100
R4	0.023393	0.021648	0.021418	0.021345	-	-	-	-	0.022942	0.022966	0.023262	0.023527	0.023196
R5	0.022400	0.022927	0.022541	0.023354		-		-	-	-	-	-	-
B1	0.273435	0.273461	0.272865	0.272714	0.272943	0.272393	0.272995	0.272623	0.271692	0.271734	0.272012	0.272599	0.271924
B2	0.317860	0.311277	0.319728	0.317411	0.309458	0.318206	0.309446	0.318756	0.323116	0.322729	0.321319	0.320467	0.321418
B3	0.427902	0.466308	0.441828	0.446186	0.466886	0.438184	0.467047	0.422168	0.377345	0.377724	0.379438	0.380238	0.379400
B4	0.325761	0.280001	0.316802	0.317229	0.274831	0.328973	0.273856	0.334485	0.282858	0.282541	0.280166	0.278642	0.280328
B5	0.288311	0.253603	0.315143	0.316698		-		-	-	-	-	-	-
B6	0.302270	0.273534	0.331881	0.264106		-		-	-	-	-	-	-
B7	0.308856	0.230466	0.293874	0.274999		-		-	-	-	-	-	-

4. Conclusions

In this study, five different benzimidazole derivatives azo dyes and five different benzothiazole derivatives Schiff base derivatives were synthesized. Some GCRPs of the compounds were calculated and possible reaction properties were determined. No linear relationship was observed between the tautomeric transitions and the electronic energy of the compounds. However, E_g was calculated lower for tautomers with intermolecular interacting hydrogens. A moderately high correlation was observed between the electronegativity and electrophilic indices of the compounds, indicating that especially HOMO energy values can be used to directly predict the reactivity of a compound. IRI surfaces overlap with QTAIM data, highlighting the usefulness of IRI calculations, which are easier than QTAIM calculations. In addition, IRI calculations reveal intense intramolecular interactions in compounds. Intramolecular interactions reduce the freedom of compounds to dihedral rotations and this may be one of the reasons why the emission peaks come at low wavelengths.

Competing Interest / Conflict of Interest

The authors declare that they have no competing interests.

Author Contribution

We declare that all Authors equally contribute.

Acknowledgements

The authors are grateful to the Scientific Research Projects Council of Kastamonu University (KÜ-BAP01/2017-31).

5. References

[1] Anthony, R. P., Rodrigo, V.D., Louis, S.K., John, C.D., & Leroy, B.T. (1998). Design, synthesis, and antiviral evaluations of 1-(Substitutedbenzyl)-2-substituted-5,6 dichlorobenzimidazoles as nonnucleoside analogues of 2,5,6-Trichloro-1-(b-D ribofuranosyl) benzimidazole. Journal of Medicinal Chemistry. 41(8), 1252-1262.

[2] Bansal, Y., & Silakari, O. (2012). The therapeutic journey of benzimidazoles: a review. Bioorganic & Medicinal Chemistry. 20(21), 6208-6236.

[3] Bishop, B.C., Chelton, E.T.J., & Jones, A.S. (1964). Biochemical Pharmacology. 13(5), 751-754.

[4] Habib, N.S., Soliman, R., Ashoura, F.A., & El-Taiebi, M. (1997). Synthesis and antimicrobial testing of novel oxadiazolylbenzimidazole derivatives. Die Pharmazie, 52(10), 746-749.

[5] Tuncbilek, M., Goker, H., Ertan, R., Eryigit, R., Kendi, E., & Altanlar, E. (1997). Synthesis and antimicrobial activity of some new anilino benzimidazoles. Archiv der Pharmazie, 330(12), 372-376.

[6] Göker, H., Tunçbilek, M., Süzen, S., Kus, C., & Altanlar, N. (2001). Synthesis and Antimicrobial Activity of Some New 2-Phenyl-N-substituted Carboxamido-1H-benzimidazole Derivatives. Archiv der Pharmazie: An International Journal Pharmaceutical and Medicinal Chemistry, 334(5), 148-152.

[7] Göker, H., Kuş, C., Boykin, D. W., Yildiz, S., & Altanlar, N. (2002). Synthesis of some new 2-substituted-phenyl-1H-benzimidazole-5-carbonitriles and their potent activity against Candida species. Bioorganic & medicinal chemistry, 10(8), 2589-2596.

[8] Pawar, N. S., Dalal, D. S., Shimpi, S. R., & Mahulikar, P. P. (2004). Studies of antimicrobial activity of N-alkyl and N-acyl 2-(4-thiazolyl)-1H-benzimidazoles. European journal of pharmaceutical sciences, 21(2-3), 115-118.

[9] Mohamed, B. G., Hussein, M. A., Abdel-Alim, A. A. M., & Hashem, M. (2006). Synthesis and antimicrobial activity of some new 1-alkyl-2-alkylthio-1, 2, 4-triazolobenzimidazole derivatives. Archives of pharmacal research, 29, 26-33.

[10] Vaidya, S. D., Kumar, B. V. S., Kumar, R. V., Bhise, U. N., & Mashelkar, U. C. (2007). Synthesis, anti-bacterial, anti-asthmatic and anti-diabetic activities of novel N-substituted-2-(benzo [d] isoxazol-3-ylmethyl)-1H-benzimidazoles. Journal of heterocyclic chemistry, 44(3), 685-691.

[11] Hogale, M. B., Uthale, A. C., & Nikam, B. P. (1991). hydrazidophenothiazines (IV). These intermediate inhibitory concentration (MIC) in mg/ml. The MIC. Indian Journal of Chemistry: Organic including medicinal. Section B, 30, 717-720.

[12] Srivastava, S. K., Srivastava, S., & Srivastava, S. D. (2002). Synthesis of new 1, 2, 4-triazolo-thiadiazoles and its 2-oxoazetidines as antimicrobial, anticonvulsant and antiinflammatory agents. Indian Journal of Chemistry. 41B, 2357-2363.

[13] Desai, K. G., & Desai, K. R. (2006). Green route for the heterocyclization of 2-mercaptobenzimidazole into β-lactum segment derivatives containing–CONH–bridge with benzimidazole: Screening in vitro antimicrobial activity with various microorganisms. Bioorganic and medicinal chemistry, 14(24), 8271-8279.

[14] Furniss, B.S., Hannaford, A.J., Smith, P.W.G., & Tatchell, A.R. (Eds.) (1998). Vogel's Text Book of Practical Organic Chemistry. ELBS Longman, England.

[15] Gür, M., Yerlikaya, S., Şener, N., Özkınalı, S., Baloglu, M. C., Gökçe, H., ... & Şener, İ. (2020). Antiproliferative-antimicrobial properties and structural analysis of newly synthesized Schiff bases derived from some 1, 3, 4-thiadiazole compounds. Journal of Molecular Structure, 1219, 128570.

[16] Ashour, F. A., Habib, N. S., El Taibbi, M., El Dine, S., & El Dine, A. S. (1990). Synthesis of 1, 3, 4-thiadiazoles, imidazo [2, 1-b] 1, 3, 4-thiadiazoles and thiadiazolo [3, 2-a] pyrimidines derived from benzimidazole as potential antimicrobial agents. Farmaco (Societa Chimica Italiana: 1989), 45(12), 1341-1349.

[17] Habib, N. S., Soliman, R., Ashour, F. A., & El-Taiebi, M. (1997). Synthesis and antimicrobial testing of 4H-1, 2, 4-triazole, 1, 2, 4-triazolo [3, 4-b][1, 3, 4] thiadiazole and 1, 2, 4-triazolo [3, 4-b][1, 3, 4] thiadiazine derivatives of 1H-benzimidazole. Die Pharmazie, 52(11), 844.

[18] Valeur, B., & Brochon, J. C. (Eds.). (2012). New trends in fluorescence spectroscopy: applications to chemical and life sciences (Vol. 1). Springer Science & Business Media.

[19] Strianese, M., Staiano, M., Ruggiero, G., Labella, T., Pellecchia, C., & D'Auria, S. (2012). Fluorescence-based biosensors. Spectroscopic methods of analysis: methods and protocols, 193-216.

[20] Goldys, E. M. (2009). Fluorescence applications in biotechnology and life sciences. John Wiley & Sons.

[21] Kraayenhof, R., Visser, A. J., & Gerritsen, H. C. (Eds.). (2012). Fluorescence spectroscopy, imaging and probes: new tools in chemical, physical and life sciences (Vol. 2). Springer Science & Business Media.

[22] Kalauzi, A., Mutavdžić, D., Djikanović, D., Radotić, K., & Jeremić, M. (2007). Application of asymmetric model in analysis of fluorescence spectra of biologically important molecules. Journal of fluorescence, 17(3), 319-329.

[23] Hunger, K. (Ed.). (2007). Industrial dyes: chemistry, properties, applications. John Wiley & Sons.

[24] Zollinger, H. (2003). Color chemistry: syntheses, properties, and applications of organic dyes and pigments. John Wiley & Sons.

[25] Kasture, P. P., Sonawane, Y. A., Rajule, R. N., & Shankarling, G. S. (2010). Synthesis and characterisation of benzothiazole-based solid-state fluorescent azo dyes. Coloration Technology, 126(6), 348-352.

[26] Ncube, P., Krause, R. W., & Mamba, B. B. (2011). Fluorescent sensing of chlorophenols in water using an azo dye modified β-cyclodextrin polymer. Sensors, 11(5), 4598-4608.

[27] Wolfbeis, O. S. (2005). Materials for fluorescence-based optical chemical sensors. Journal of Materials Chemistry, 15(27-28), 2657-2669.

[28] Lee, L. G., Taing, M. C., & Rosenblum, B. B. (2006). U.S. Patent No. 7,038,063. Washington, DC: U.S. Patent and Trademark Office.

[29] Chen, C. H., Liao, D. J., Wan, C. F., & Wu, A. T. (2013). A turn-on and reversible Schiff base fluorescence sensor for Al 3+ ion. Analyst, 138(9), 2527-2530.

[30] Hsieh, W. H., Wan, C. F., Liao, D. J., & Wu, A. T. (2012). A turn-on Schiff base fluorescence sensor for zinc ion. Tetrahedron letters, 53(44), 5848-5851.

[31] Guo, L., Wu, S., Zeng, F., & Zhao, J. (2006). Synthesis and fluorescence property of terbium complex with novel schiff-base macromolecular ligand. European polymer journal, 42(7), 1670-1675.

[32] Kohn, W., & Sham, L.J. (1965). Self-consistent equations including exchange and correlation effects. Physical Review. 140 (4A), 1133-1138.

[33] Hohenberg, P., & Kohn, W. (1964). Inhomogeneous Electron Gas, Physical Review. 136(3B), 864-871.

[34] Frisch, M., Trucks, G., & Schlegel, H. (2009). G.S.-G. 09, Gaussian, Inc., Wallingford CT.
[35] Bader, R. F. (1991). A quantum theory of molecular structure and its applications. Chemical Reviews, 91(5), 893-928.
[36] Bader, R. F. (1985). Atoms in molecules. Accounts of Chemical Research, 18(1), 9-15.
[37] Lu, T., & Chen, F. (2012). Multiwfn: A multifunctional wavefunction analyzer. Journal of computational chemistry, 33(5), 580-592.
[38] Aydogdu, S., & Hatipoglu, A. (2022). The reaction mechanism investigation of sulfonamides with OH radical by DFT. Journal of the Indian Chemical Society, 99(11), 100752.
[39] Domingo, L. R., & Pérez, P. (2011). The nucleophilicity N index in organic chemistry. Organic & biomolecular chemistry, 9(20), 7168-7175.

SUPPLEMENTARY

Table S1. Calculated electronic parameters of the compounds

Comp.	E (au)	E_{HOMO} (eV)	E_{LUMO} (eV)	ΔE (eV)	η (eV)	χ (eV)	ω (eV)	ε (eV)	α *(au)*	μ *Debye*	ω⁻ (eV)
2a	-1624.80	-6.376	-3.487	2.889	1.445	4.932	8.418	3.119	405.731	6.881	7.036
2a-T	-1624.75	-6.563	-3.213	3.350	1.675	4.888	7.132	2.932	349.324	6.231	6.429
2b	-1533.49	-5.935	-3.069	2.866	1.433	4.502	7.072	3.560	412.928	2.696	6.145
2c	-1644.64	-6.233	-2.943	3.290	1.645	4.588	6.398	3.262	368.272	2.133	5.904
2d	-1413.07	-6.570	-2.932	3.638	1.819	4.751	6.205	2.925	275.568	5.383	5.933
2d-T	-1413.08	-6.093	-2.721	3.372	1.686	4.407	5.760	3.402	302.219	3.350	5.505
2e	-1644.18	-6.185	-2.967	3.218	1.609	4.576	6.507	3.310	362.967	5.790	5.944
2e-T	-1644.20	-6.039	-2.745	3.294	1.647	4.392	5.856	3.456	406.876	2.915	7.036
3a	-1403.10	-5.917	-2.286	3.631	1.816	4.102	4.633	3.578	332.186	0.708	4.821
3b	-1363.79	-5.977	-2.336	3.641	1.821	4.157	4.745	3.518	313.569	1.221	4.906
3c	-1748.16	-6.185	-2.650	3.535	1.768	4.418	5.520	3.310	326.180	3.835	5.411
3d	-1493.11	-6.431	-3.436	2.995	1.498	4.934	8.127	3.064	340.767	8.400	6.904
3e	-1387.81	-6.160	-2.548	3.612	1.806	4.354	5.248	3.335	302.389	3.546	5.253

E: Energy, ΔE: $E_{LUMO} - E_{HOMO}$, η: Chemical Hardness, χ: Electronegativity, **ω**: Electrophilic index, **ε**: Nucleophilic index, **α:** Polarizability, μ: Dipole moment, ω⁻ : Electrodonating power.

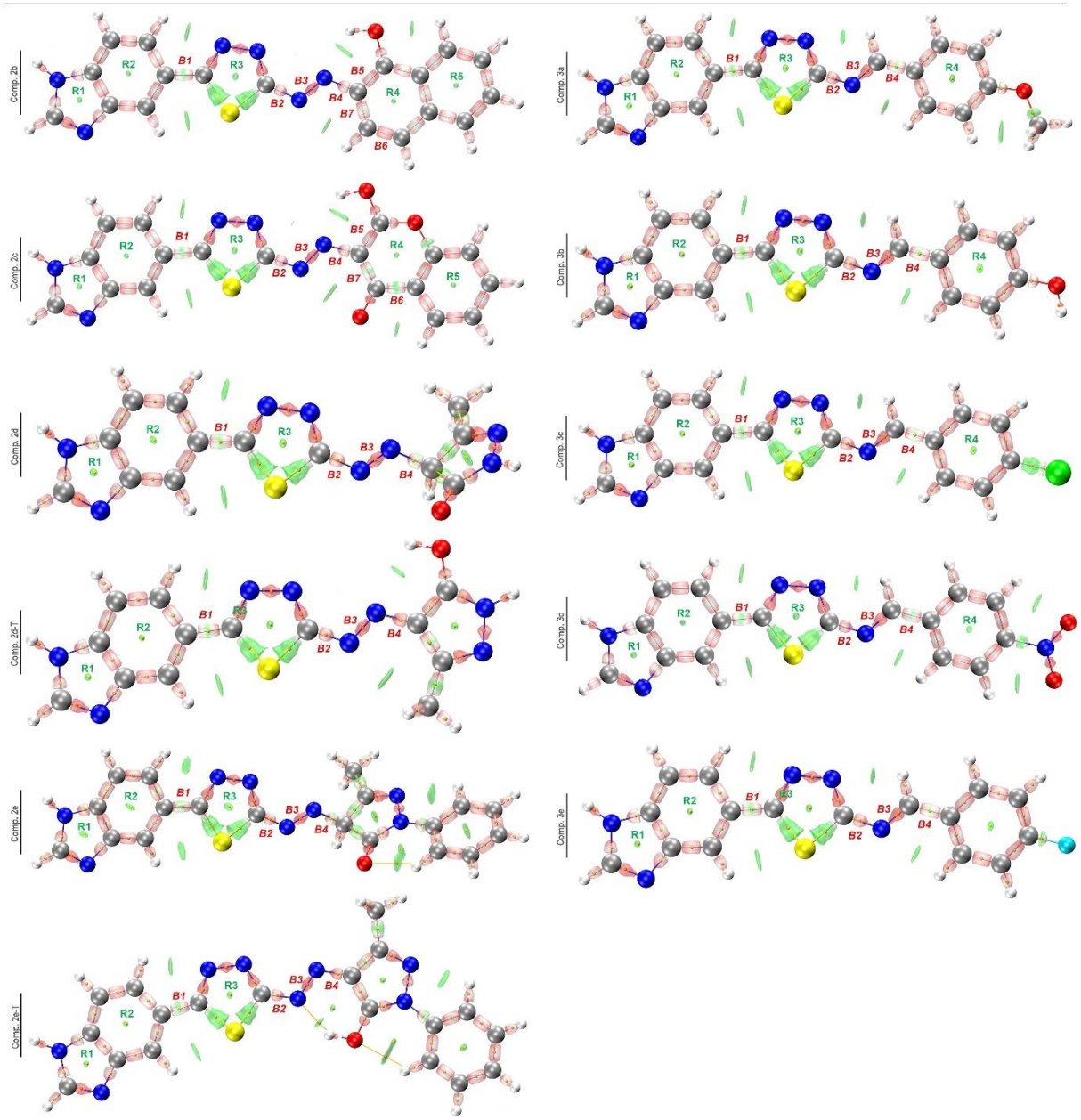

Figure S1. IRI maps of the compounds.